International Journal for Numerical Methods in Engineering

WILEY

RESEARCH ARTICLE OPEN ACCESS

A Hybrid Pressure Formulation of the Face-Centred Finite Volume Method for Viscous Laminar Incompressible Flows

Matteo Giacomini[1,2] | Davide Cortellessa[1] | Luan M. Vieira[1,2,3] | Ruben Sevilla[3] | Antonio Huerta[1,2]

[1]Laboratori de Càlcul Numèric (LaCàN), ETS de Ingeniería de Caminos, Canales y Puertos, Universitat Politècnica de Catalunya, Barcelona, Spain | [2]Centre Internacional de Mètodes Numèrics en Enginyeria (CIMNE), Barcelona, Spain | [3]Zienkiewicz Centre for Computational Engineering, Faculty of Science and Engineering, Swansea University, Wales, UK

Correspondence: Antonio Huerta (antonio.huerta@upc.edu)

Received: 16 September 2024 | **Revised:** 31 January 2025 | **Accepted:** 31 March 2025

Funding: This work was supported by the H2020 MSCA (ITN-EJD 764636), Generalitat de Catalunya (2021-SGR-01049), Agencia Estatal de Investigación and MICIU/AEI/10.13039/501100011033 (PID2020-113463RB-C33, PID2020-113463RB-C32, CEX2018-000797-S).

Keywords: face-centred | finite volume methods | hybrid methods | hybridizable discontinuous Galerkin | incompressible Navier-Stokes

ABSTRACT

This work presents a hybrid pressure face-centred finite volume (FCFV) solver to simulate steady-state incompressible Navier-Stokes flows. The method leverages the robustness, in the incompressible limit, of the hybridisable discontinuous Galerkin paradigm for compressible and weakly compressible flows to derive the formulation of a novel, low-order face-based discretization. The incompressibility constraint is enforced in a weak sense by introducing an inter-cell mass flux, defined in terms of a new, hybrid variable that represents the pressure at the cell faces. This results in a new hybridization strategy where cell variables (velocity, pressure, and deviatoric strain rate tensor) are expressed as a function of velocity and pressure at the barycentre of the cell faces. The hybrid pressure formulation provides first-order convergence of all variables, including the stress, without the need for gradient reconstruction, thus being less sensitive to cell type, stretching, distortion, and skewness than traditional low-order finite volume solvers. Numerical benchmarks of Navier-Stokes flows at low and moderate Reynolds numbers, in two and three dimensions, are presented to evaluate the accuracy and robustness of the method. In particular, the hybrid pressure formulation outperforms the FCFV method when convective effects are relevant, achieving accurate predictions on significantly coarser meshes.

1 | Introduction

Despite the increasing interest towards high-order methods for the simulation of incompressible flows [1–3], low-order approaches such as finite volume (FV) methods [4, 5] still represent the majority of available computational fluid dynamics (CFD) technologies for industrial applications.

Most existing FV codes can be classified into two groups, namely, vertex-centred (VCFV) and cell-centred (CCFV) schemes. Whilst these approaches differ in the positioning of the degrees of freedom (respectively, at mesh nodes and at cell barycentres) and in the definition of the control volume (respectively, using a dual mesh and exploiting existing mesh cells), they share common drawbacks and limitations. In particular, both techniques rely on a reconstruction of the gradient of the unknown velocity to achieve first-order convergence of the stress, and such a reconstruction is prone to experience a significant loss of accuracy in the presence of distorted or stretched cells [6, 7].

Davide Cortellessa and Luan M. Vieira are listed in alphabetical order and have contributed equally to the work.

To circumvent this issue, a new FV paradigm [8] was proposed. The face-centred finite volume (FCFV) method relies on a mixed formulation of the governing equations in each cell (which acts as a control volume), localizing the degrees of freedom at the barycentre of the cell faces. The resulting method achieves first-order convergence of all the physical variables involved in the formulation, including the stress tensor, without the need to perform gradient reconstruction, thus being less sensitive to cell stretching and distortion with respect to traditional FV approaches.

Besides Poisson and Stokes equations [8], FCFV solvers have been successfully developed for linear elasticity [9], high-contrast and variable viscosity Stokes flows [10, 11], viscous laminar and inviscid compressible flows [12, 13], and viscous laminar and turbulent incompressible flows [14, 15]. Second-order versions of the FCFV method enriched by automatic mesh adaptation strategies were also presented for linear elliptic problems [16, 17].

It is worth recalling that second-order CCFV schemes can be seen as the lowest order version of a discontinuous Galerkin (DG) method, whereas second-order VCFV methods on simplicial meshes can be interpreted as the piecewise linear approximation of a continuous Galerkin (CG) formulation on a dual mesh. In a similar fashion, the FCFV paradigm can be seen as a hybridisable discontinuous Galerkin (HDG) method [18–21] with piecewise constant approximation in each mesh cell and on each mesh face. Indeed, existing FCFV formulations for Stokes and incompressible Navier-Stokes equations were derived leveraging the knowledge on HDG for incompressible flows [22–25]. Hence, the FCFV scheme inherits from HDG its properties, including the suitability to handle different cell types, the robustness to cell stretching and distortion, as well as the stability for perfectly incompressible flows, circumventing the Ladyzhenskaya-Babuška-Brezzi (LBB) condition [26], without the need for pressure correction algorithms. In addition, FCFV mimics the hybridization procedure of HDG to express the cell unknowns (i.e., velocity, pressure, and gradient of velocity) as functions of the face velocities and the average pressure in the cell via the solution of a set of independent problems, solved cell-by-cell.

Previous works on FCFV for incompressible flows highlighted that although the method achieves first-order convergence for velocity, pressure, and gradient of velocity, the approximation of pressure is prone to experience the largest values of the error [8, 10, 11, 14]. On the contrary, HDG methods devised for compressible and weakly compressible flows [27–29] were shown to be robust, accurate, and stable in the incompressible limit [30], also when using low-order polynomials. Stemming from these observations, this work presents a novel formulation of a face-based FV solver to simulate laminar incompressible Navier-Stokes flows. The method relies on a new hybridization procedure such that (i) a new face variable is introduced to represent the trace of pressure on the cell faces, (ii) mass conservation is enforced weakly (instead of strongly cell-by-cell), leading to an extra integral equation in each cell, and (iii) a suitable definition of the inter-cell mass flux in terms of the newly introduced *hybrid pressure* is provided.

The three points mentioned above mark the difference between the hybrid pressure formulation and the FCFV method for laminar incompressible Navier-Stokes proposed by Vieira et al. [14], where pressure is defined exclusively inside each cell and incompressibility is enforced strongly. On the contrary, to introduce the new hybrid pressure, mass conservation can only be imposed weakly. Nonetheless, it is worth noticing that upon mesh refinement, the pressure defined in each cell converges to the hybrid pressure, thus guaranteeing that the flow is perfectly incompressible and mass conservation is verified up to machine precision. The resulting hybrid pressure formulation thus outperforms the FCFV method, achieving superior accuracy for pressure and aerodynamic forces using coarser meshes, especially when convection phenomena are involved. The proposed method is also closely related to the high-order HDG formulations that first introduced face unknowns for pressure [31–33]. The novelties of the presented approach with respect to these works are the use of a mixed formulation with a symmetric mixed variable, the discretization of all variables with the same degree of approximation (i.e., constant functions in the cells and on the faces), and the inclusion of Riemann solvers in the definition of the stabilization strategy for convection.

The remainder of this article is organized as follows. Section 2 recalls the governing equations for a viscous laminar incompressible flow. Section 3 introduces the new hybridization procedure and derives the integral form of the hybrid pressure FCFV method for the incompressible Navier-Stokes equations. The discrete problem and the corresponding nonlinear solver are described in Section 4, whereas Section 5 provides some considerations on the computational aspects and the numerical properties of the method. Numerical examples, including academic test cases, as well as two- and three-dimensional benchmark problems for Navier-Stokes flows at low and moderate Reynolds numbers, are presented in Section 6. Finally, Section 7 summarizes the results of this work, whereas technical implementation aspects and the hybrid pressure formulation for the Stokes equations are presented in Appendices A and B, respectively.

2 | Governing Equations for Viscous Laminar Incompressible Flows

Let $\Omega \subset \mathbb{R}^{\mathrm{n_{sd}}}$ be an open, bounded computational domain in $\mathrm{n_{sd}}$ spatial dimensions, with boundary $\partial\Omega = \Gamma_D \cup \Gamma_N \cup \Gamma_S$ such that Γ_D, Γ_N, and Γ_S are disjoint by pairs. Denoting by $(\boldsymbol{u}, p)$ the velocity-pressure pair, the steady-state incompressible Navier-Stokes equations are given by

$$\begin{cases} -\boldsymbol{\nabla}\cdot\boldsymbol{\sigma} + \boldsymbol{\nabla}\cdot(\boldsymbol{u}\otimes\boldsymbol{u}) = \boldsymbol{s} & \text{in } \Omega, \\ \boldsymbol{\nabla}\cdot\boldsymbol{u} = 0 & \text{in } \Omega, \\ \boldsymbol{B}(\boldsymbol{\varepsilon}^d, \boldsymbol{u}, p) = \boldsymbol{0} & \text{on } \partial\Omega \end{cases} \tag{1}$$

where $\boldsymbol{s}$ is the body force, $\boldsymbol{B}$ denotes an operator enforcing the boundary conditions, and $\boldsymbol{\sigma}$ is the Cauchy stress tensor. For a Newtonian fluid under Stokes' hypothesis, the stress tensor is written as $\boldsymbol{\sigma} = -p\mathbf{I}_{\mathrm{n_{sd}}} + \boldsymbol{\sigma}^d$, where $\mathbf{I}_{\mathrm{n_{sd}}}$ is the identity matrix of dimension $\mathrm{n_{sd}} \times \mathrm{n_{sd}}$, $\boldsymbol{\sigma}^d = \nu\boldsymbol{\varepsilon}^d$ is the deviatoric stress tensor, and

$$\boldsymbol{\varepsilon}^d := 2\boldsymbol{\nabla}^{\mathrm{s}}\boldsymbol{u} - \frac{2}{3}(\boldsymbol{\nabla}\cdot\boldsymbol{u})\mathbf{I}_{\mathrm{n_{sd}}} \tag{2}$$

is the deviatoric strain rate tensor, $\boldsymbol{\nabla}^{\mathrm{s}} := (\boldsymbol{\nabla} + \boldsymbol{\nabla}^T)/2$ being the symmetric part of the gradient operator. Finally, ν represents the kinematic viscosity of the fluid. Under the assumption of unitary characteristic length and unitary characteristic velocity, the viscosity is set equal to the inverse of the Reynolds number Re, i.e., $\nu = 1/Re$.

Remark 1. Equation (2) is usually simplified by imposing that the velocity is pointwise divergence-free, thus neglecting the last term in the definition of $\boldsymbol{\varepsilon}^d$. Nonetheless, the numerical formulation presented in this work enforces the incompressibility equation only in a weak sense, and the term proportional to $\boldsymbol{\nabla} \cdot \boldsymbol{u}$ is thus preserved in Equation (2) and the following derivation.

The governing Equation (1) are finally closed by means of a set of boundary conditions, see Equation (3), setting the value $\boldsymbol{u}_D$ of the velocity on the Dirichlet boundary Γ_D, the traction $\boldsymbol{g}$ on the Neumann portion Γ_N, whereas a perfectly slip and a non-penetration conditions are imposed on the symmetry contour Γ_S, i.e.,

$$\boldsymbol{B}(\boldsymbol{\varepsilon}^d, \boldsymbol{u}, p) := \begin{cases} \boldsymbol{u} - \boldsymbol{u}_D & \text{on } \Gamma_D, \\ -p\boldsymbol{n} + \nu\boldsymbol{\varepsilon}^d\boldsymbol{n} - \boldsymbol{g} & \text{on } \Gamma_N, \\ \begin{Bmatrix} \boldsymbol{t}_k \cdot \nu\boldsymbol{\varepsilon}^d\boldsymbol{n} \\ \boldsymbol{u} \cdot \boldsymbol{n} \end{Bmatrix} & \text{on } \Gamma_S, \text{ for } k = 1, \ldots, \mathtt{n_{sd}} - 1 \end{cases} \tag{3}$$

where the outward unit normal vector $\boldsymbol{n}$ and the unit tangential vectors $\boldsymbol{t}_k, k = 1, \ldots, \mathtt{n_{sd}} - 1$ form an orthonormal system of vectors. In this work, outflow boundaries are modeled using homogeneous Neumann conditions. For further details, Giacomini et al. [30] present a numerical study of different conditions suitable for outlet boundaries.

Finally, recall that the compatibility condition

$$\int_{\Gamma_D} \boldsymbol{u}_D \cdot \boldsymbol{n} \, d\Gamma + \int_{\partial\Omega \setminus \Gamma_D} \boldsymbol{u} \cdot \boldsymbol{n} \, d\Gamma = 0 \tag{4}$$

stems from the divergence-free condition on the velocity field in Ω. Moreover, if $\Gamma_N = \emptyset$, an additional constraint, e.g.,

$$\int_{\Omega} p \, d\Omega = 0 \tag{5}$$

needs to be introduced to eliminate the indeterminacy of the pressure field [34].

3 | Foundations of the FCFV Method With Hybrid Pressure

The domain Ω is subdivided into a set of $\mathtt{n_{el}}$ non-overlapping cells $\Omega_e, e = 1, \ldots, \mathtt{n_{el}}$. The boundary $\partial\Omega_e$ of each cell consists of a set of $\mathtt{n}^e_{\mathtt{fa}}$ faces $\Gamma_{e,j}, j = 1, \ldots, \mathtt{n}^e_{\mathtt{fa}}$, with $\mathtt{n}^e_{\mathtt{fa}}$ varying depending on the type of cell Ω_e. Moreover, the collection of all the faces, excluding the ones on the boundary of the domain, defines the internal interface (also known as *internal mesh skeleton*)

$$\Gamma := [\bigcup_{e=1}^{\mathtt{n_{el}}} \partial\Omega_e] \setminus \partial\Omega \tag{6}$$

Remark 2. Note that previous works [8, 17] showed the ability of the FCFV framework to seamlessly handle meshes of triangles, quadrilaterals, tetrahedra, hexahedra, prisms, and pyramids, as well as hybrid meshes consisting of different cell types. For the sake of brevity, in this work, meshes of quadrilaterals and triangles will be employed in 2D, whereas only tetrahedral cells will be considered in 3D.

Similarly to the FCFV method introduced by Sevilla et al. [8] and successively studied for different physical problems [9–14], the FCFV formulation with hybrid pressure is constructed starting from a series of ingredients:

- a mixed, hybrid formulation of the equations;
- a piecewise constant approximation of the unknowns in the cells and on the faces;
- a definition of the numerical fluxes to handle inter-cell communication;
- a hybridization (or *static condensation*) step to eliminate cell unknowns, expressing them in terms of face unknowns.

At the same time, several novelties are introduced by the hybrid pressure FCFV method. First, whilst most of the above cited references rely on a velocity-pressure formulation of the Stokes and Navier-Stokes equations, the present work derives the mixed problem starting from a Cauchy formulation of the momentum equation and imposes the symmetry of the mixed variable pointwise [25, 30, 35]. Second, besides the piecewise constant approximation of velocity, pressure, and deviatoric strain rate tensor in each cell, and the piecewise constant approximation of velocity on the cell faces, the proposed approach introduces a new, additional hybrid variable representing the trace of the pressure, also defined on the cell faces. A schematic representation of the degrees of freedom of the hybrid pressure formulation and FCFV method is displayed in Figure 1.

Moreover, the mass conservation equation is imposed in a weak sense, entailing the need to appropriately define an inter-cell mass flux, which is expressed in terms of the newly introduced hybrid pressure variable. Finally, a new hybridization strategy is proposed to express the cell unknowns as functions of the hybrid variables (i.e., face velocity and face pressure) via the solution of a set of independent problems, solved cell-by-cell. The following subsections detail the building blocks of the hybrid pressure formulation.

3.1 | Mixed Hybrid Formulation

Stemming from the rationale of HDG proposed by Cockburn and co-workers [18, 19, 23, 36, 37], the FCFV method with hybrid pressure employs a mixed formulation of the problem via the introduction of $\boldsymbol{L} = -\boldsymbol{\varepsilon}^d$ as a mixed variable.

Remark 3. By construction, the mixed variable $\boldsymbol{L}$ is symmetric. For convenience, Voigt notation is employed to enforce pointwise symmetry at the discrete level, storing only the non-redundant components of the tensor. An overview of the technical details is provided in Appendix A, whereas a more extensive discussion on the topic was presented by Giacomini et al. [30].

Upon introducing the new, hybrid variables $\hat{\boldsymbol{u}}$ on $\Gamma \cup \Gamma_N \cup \Gamma_S$ and $\hat{p}$ on $\Gamma \cup \partial\Omega$, respectively representing the trace of velocity and

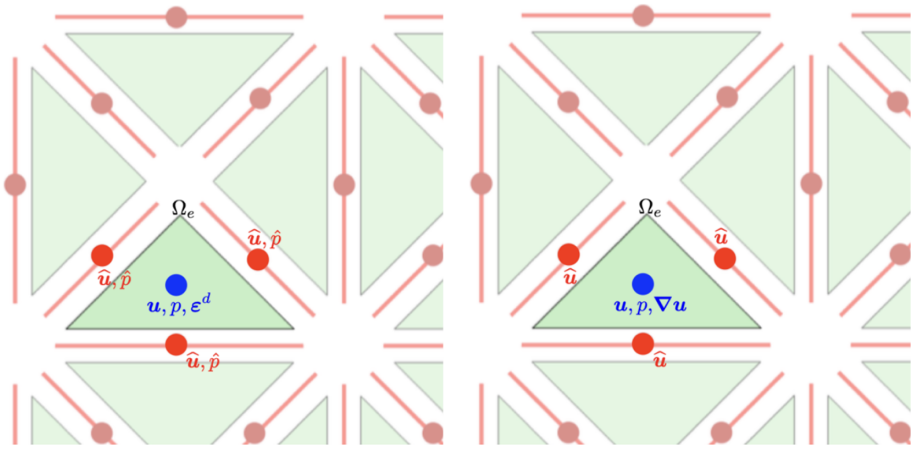

FIGURE 1 | Degrees of freedom of (a) hybrid pressure and (b) FCFV methods for cell Ω_e. $\boldsymbol{u}$: Cell velocity, p: Cell pressure, $\boldsymbol{\varepsilon}^d$: Cell deviatoric strain rate tensor, $\nabla \boldsymbol{u}$: Cell velocity gradient tensor, $\widehat{\boldsymbol{u}}$: Face velocity, and $\hat{p}$: Face pressure.

pressure at the cell faces, problem (1) can be rewritten in each cell Ω_e, for $e = 1, \ldots, \mathtt{n_{el}}$, as

$$\begin{cases} \boldsymbol{L} + 2\nabla^{\mathrm{s}}\boldsymbol{u} - \dfrac{2}{3}(\nabla \cdot \boldsymbol{u})\mathbf{I}_{\mathtt{n_{sd}}} = \mathbf{0} & \text{in } \Omega_e, \\ \nabla \cdot (\nu \boldsymbol{L}) + \nabla \cdot (p\mathbf{I}_{\mathtt{n_{sd}}} + \boldsymbol{u} \otimes \boldsymbol{u}) = \boldsymbol{s} & \text{in } \Omega_e, \\ \nabla \cdot \boldsymbol{u} = 0 & \text{in } \Omega_e, \\ \boldsymbol{u} = \boldsymbol{u}_D & \text{on } \partial\Omega_e \cap \Gamma_D, \\ \boldsymbol{u} = \widehat{\boldsymbol{u}} & \text{on } \partial\Omega_e \setminus \Gamma_D \end{cases} \tag{7}$$

while imposing the boundary conditions on $\Gamma_N \cup \Gamma_S$ and the inter-cell continuity of momentum flux on the interior faces Γ,

$$\begin{cases} \boldsymbol{B}(-\boldsymbol{L}, \boldsymbol{u}, p) = \mathbf{0} & \text{on } \partial\Omega \setminus \Gamma_D, \\ [\![\left(\nu \boldsymbol{L} + p\mathbf{I}_{\mathtt{n_{sd}}} + \boldsymbol{u} \otimes \boldsymbol{u}\right) \boldsymbol{n}]\!] = \mathbf{0} & \text{on } \Gamma \end{cases} \tag{8}$$

as well as the inter-cell continuity of velocity on Γ, i.e.,

$$[\![\boldsymbol{u} \otimes \boldsymbol{n}]\!] = \mathbf{0} \qquad \text{on } \Gamma \tag{9}$$

Note that, in Equations (8) and (9), the jump operator is defined as $[\![\odot]\!] := \odot_{\mathtt{l}} + \odot_{\mathtt{r}}$ by summing the contributions $\odot_{\mathtt{l}}$ and $\odot_{\mathtt{r}}$ of the cells $\Omega_{\mathtt{l}}$ and $\Omega_{\mathtt{r}}$ sharing the interface Γ, including the outward normal vectors $\boldsymbol{n}_{\mathtt{l}}$ and $\boldsymbol{n}_{\mathtt{r}}$, respectively [38]. It is straightforward to verify that this notation allows us to rewrite (9) on each face in Γ as

$$\mathbf{0} = [\![\boldsymbol{u} \otimes \boldsymbol{n}]\!] = \boldsymbol{u}_{\mathtt{l}} \otimes \boldsymbol{n}_{\mathtt{l}} + \boldsymbol{u}_{\mathtt{r}} \otimes \boldsymbol{n}_{\mathtt{r}} = (\boldsymbol{u}_{\mathtt{l}} - \boldsymbol{u}_{\mathtt{r}}) \otimes \boldsymbol{n}_{\mathtt{l}} \tag{10}$$

where the last equality holds because $\boldsymbol{n}_{\mathtt{r}} = -\boldsymbol{n}_{\mathtt{l}}$, thus enforcing the expected inter-cell continuity of the velocity field on any arbitrarily oriented mesh face.

To have a unique solution, problem (7) requires, for each cell, compatible velocities along its faces and an additional condition to handle the indeterminacy of pressure. Both restrictions are imposed weakly by means of (8) and (9), as will be detailed in the upcoming subsections. Consequently, for every cell Ω_e, it is assumed that the hybrid velocity is compatible with the cell velocity via the boundary conditions in Equation (7), and that the hybrid pressure, employed to weakly enforce cell-by-cell incompressibility, is such that $\hat{p} = p$ on $\partial\Omega_e$ removing the indeterminacy of the cell pressure.

Moreover, it is worth noticing that Equation (9) can be rewritten in terms of the orthonormal system of vectors $\{\boldsymbol{n}, \boldsymbol{t}_1, \ldots, \boldsymbol{t}_{\mathtt{n_{sd}}-1}\}$ representing the normal and tangential directions to the internal mesh edges ($\mathtt{n_{sd}} = 2$) or faces ($\mathtt{n_{sd}} = 3$). More specifically, the inter-cell continuity of the velocity is equivalent to

$$\begin{cases} [\![\boldsymbol{u} \cdot \boldsymbol{n}]\!] = 0 & \text{on } \Gamma, \\ (\boldsymbol{u}_{\mathtt{l}} - \boldsymbol{u}_{\mathtt{r}}) \cdot \boldsymbol{t}_k = 0 & \text{on } \Gamma, \text{ for } k = 1, \ldots, \mathtt{n_{sd}} - 1 \end{cases} \tag{11}$$

The first equation in Equation (11) enforces the continuity of the normal component of the velocity of two neighboring cells across the interface Γ (i.e., mass conservation), whereas the remaining $\mathtt{n_{sd}} - 1$ equations enforce continuity of the tangential components of the velocity, i.e., absence of shear effects on internal mesh faces.

Given the uniqueness of $\widehat{\boldsymbol{u}}$ on the faces of the internal mesh skeleton and the condition imposed on $\boldsymbol{u}$ at the cell boundaries in Equation (7), the continuity of the tangential component of the velocity is automatically fulfilled. On the contrary, the continuity of the mass flux across Γ, represented by the first equation in Equation (11), does not follow straightforwardly as in traditional formulations of hybrid methods [8, 30]. Indeed, the relaxation of the incompressibility constraint (see Remark 1) is responsible for the velocity to not fulfill strongly such an equation and for the normal component of $\boldsymbol{u}$ to violate the condition prescribed at the cell boundaries in problem (7). Hence, the hybrid pressure FCFV method needs to explicitly enforce the continuity of the mass flux on Γ and the appropriate value of the normal component of the velocity on $\partial\Omega$, i.e., Equation (8) is to be complemented with

$$\begin{cases} \boldsymbol{u} \cdot \boldsymbol{n} = \boldsymbol{u}_D \cdot \boldsymbol{n} & \text{on } \partial\Omega \cap \Gamma_D, \\ \boldsymbol{u} \cdot \boldsymbol{n} = \widehat{\boldsymbol{u}} \cdot \boldsymbol{n} & \text{on } \partial\Omega \setminus \Gamma_D, \\ [\![\boldsymbol{u} \cdot \boldsymbol{n}]\!] = \mathbf{0} & \text{on } \Gamma \end{cases} \tag{12}$$

Following the FCFV rationale, the solution strategy for the hybrid pressure formulation relies on two steps: First, the so-called local Equation (7) is solved cell-by-cell to express the cell unknowns as a function of the face unknowns, i.e., $\widehat{\boldsymbol{u}}$ and $\hat{p}$ (*hybridization* step); then, the face variables are determined solving the so-called global problem to enforce Equations (8) and (12) (*equilibration* step).

3.2 | Integral Form of the Local Problem

The hybridization step is obtained by applying the divergence theorem to (7), yielding the integral form of the local problem

$$\begin{cases} \int_{\Omega_e} \boldsymbol{L}\, d\Omega + \int_{\partial\Omega_e\cap\Gamma_D} \left(\boldsymbol{u}_D\otimes\boldsymbol{n} + \boldsymbol{n}\otimes\boldsymbol{u}_D - \frac{2}{3}(\boldsymbol{u}_D\cdot\boldsymbol{n})\mathbf{I}_{\mathrm{n_{sd}}}\right) d\Gamma \\ \qquad + \int_{\partial\Omega_e\setminus\Gamma_D} \left(\widehat{\boldsymbol{u}}\otimes\boldsymbol{n} + \boldsymbol{n}\otimes\widehat{\boldsymbol{u}} - \frac{2}{3}(\widehat{\boldsymbol{u}}\cdot\boldsymbol{n})\mathbf{I}_{\mathrm{n_{sd}}}\right) d\Gamma \quad = \mathbf{0}, \\ \int_{\partial\Omega_e} (\widehat{\nu\boldsymbol{L}\boldsymbol{n}} - \nu\boldsymbol{L}\boldsymbol{n})\, d\Gamma + \int_{\partial\Omega_e} \hat{p}\boldsymbol{n}\, d\Gamma + \int_{\partial\Omega_e} \widehat{(\boldsymbol{u}\otimes\boldsymbol{u})\boldsymbol{n}}\, d\Gamma = \int_{\Omega_e} \boldsymbol{s}\, d\Omega, \\ \qquad\qquad \int_{\partial\Omega_e} \widehat{\boldsymbol{u}\cdot\boldsymbol{n}}\, d\Gamma = 0 \end{cases} \tag{13}$$

where the hybrid variables $\widehat{\boldsymbol{u}}$ and $\hat{p}$ represent the traces of velocity and pressure on the cell faces. Moreover, $\widehat{\odot}$ denotes the trace, defined on the mesh skeleton, of the numerical flux of quantity $\odot$, and it will be detailed in Section 3.4.

Note that, in Equation (13), the divergence theorem is applied twice to the viscous flux in the momentum equation and once to the gradient of pressure and the convective fluxes in the momentum equation and to the mass flux in the continuity equation. This choice yields the appearance of the difference between the numerical and the physical fluxes when the divergence theorem is applied twice, allowing for a significant simplification of the hybridization step by decoupling the computation of the three variables involved in the local problem (see Section 4.1). A detailed discussion on the double application of the divergence theorem to the viscous part of the momentum equation was presented for the FCFV method by Sevilla and Duretz [11].

As mentioned in the previous section, although problem (7) features only Dirichlet conditions on the boundary of the cell, pressure is not underdetermined in Ω_e using this formulation, under the assumption that the face pressure $\hat{p}$ matches the cell pressure p on $\partial\Omega_e$. This requirement arises from the compatibility condition enforcing incompressibility at the cell level, i.e., the third equation in Equation (13). It is worth noticing that the weak imposition of mass conservation in such an equation needs to be complemented by an appropriate definition of the inter-cell mass flux $\widehat{\boldsymbol{u}\cdot\boldsymbol{n}}$, as detailed in Section 3.4.

Hence, the solution of the local problem (13) provides the cell variables $(\boldsymbol{L}, \boldsymbol{u}, p)$ in terms of the velocity $\widehat{\boldsymbol{u}}$ and pressure $\hat{p}$ defined on the mesh faces, which are then determined by solving the global problem described in the following subsection.

3.3 | Integral Form of the Global Problem

The equilibration step determines the hybrid velocity-pressure pair $(\widehat{\boldsymbol{u}}, \hat{p})$ on the mesh faces by solving Equations (8) and (12). More precisely, the global problem enforces the boundary conditions and the inter-cell continuity of momentum flux, as in traditional hybrid methods,

$$\sum_{e=1}^{\mathrm{n_{el}}} \left\{ \int_{\partial\Omega_e\setminus\partial\Omega} \widehat{\nu\boldsymbol{L}\boldsymbol{n}}\, d\Gamma + \int_{\partial\Omega_e\setminus\partial\Omega} \hat{p}\boldsymbol{n}\, d\Gamma + \int_{\partial\Omega_e\setminus\partial\Omega} \widehat{(\boldsymbol{u}\otimes\boldsymbol{u})\boldsymbol{n}}\, d\Gamma + \int_{\partial\Omega_e\cap\partial\Omega\setminus\Gamma_D} \hat{\boldsymbol{B}}(\boldsymbol{L},\boldsymbol{u},\widehat{\boldsymbol{u}},\hat{p})\, d\Gamma \right\} = \mathbf{0} \tag{14a}$$

together with the inter-cell continuity of mass flux and the normal component of the velocity on the external boundary, i.e.,

$$\sum_{e=1}^{\mathrm{n_{el}}} \left\{ \int_{\partial\Omega_e\setminus\partial\Omega} \widehat{\boldsymbol{u}\cdot\boldsymbol{n}}\, d\Gamma + \int_{\partial\Omega_e\cap\Gamma_D} (\widehat{\boldsymbol{u}\cdot\boldsymbol{n}} - \boldsymbol{u}_D\cdot\boldsymbol{n}) d\Gamma + \int_{\partial\Omega_e\cap\partial\Omega\setminus\Gamma_D} (\widehat{\boldsymbol{u}\cdot\boldsymbol{n}} - \widehat{\boldsymbol{u}}\cdot\boldsymbol{n}) d\Gamma \right\} = 0 \tag{14b}$$

The last term in Equation (14a) represents the hybrid version of the boundary operator $\boldsymbol{B}$ defined in Equation (3), and it will be detailed in the following subsection. Indeed, to fully characterise the local and global problems presented above, appropriate definitions of all traces of the numerical fluxes are to be introduced.

3.4 | Numerical Fluxes and Convection Stabilization Inspired by Riemann Solvers

The numerical traces of the viscous and convective fluxes [12–14] are defined as

$$\widehat{\nu\boldsymbol{L}\boldsymbol{n}} := \begin{cases} \nu\boldsymbol{L}\boldsymbol{n} + \boldsymbol{\tau}^d(\boldsymbol{u}-\boldsymbol{u}_D) & \text{on } \partial\Omega_e\cap\Gamma_D, \\ \nu\boldsymbol{L}\boldsymbol{n} + \boldsymbol{\tau}^d(\boldsymbol{u}-\widehat{\boldsymbol{u}}) & \text{elsewhere} \end{cases} \tag{15a}$$

$$\widehat{(\boldsymbol{u}\otimes\boldsymbol{u})\boldsymbol{n}} := \begin{cases} (\boldsymbol{u}_D\otimes\boldsymbol{u}_D)\boldsymbol{n} + \boldsymbol{\tau}^a(\boldsymbol{u}-\boldsymbol{u}_D) & \text{on } \partial\Omega_e\cap\Gamma_D, \\ (\widehat{\boldsymbol{u}}\otimes\widehat{\boldsymbol{u}})\boldsymbol{n} + \boldsymbol{\tau}^a(\boldsymbol{u}-\widehat{\boldsymbol{u}}) & \text{elsewhere} \end{cases} \tag{15b}$$

with $\boldsymbol{\tau}^d$ and $\boldsymbol{\tau}^a$ being appropriately defined stabilization coefficients. Moreover, since the incompressibility equation is only enforced in a weak sense in the present formulation, the numerical trace of the mass flux needs to be introduced

$$\widehat{\boldsymbol{u}\cdot\boldsymbol{n}} := \begin{cases} \boldsymbol{u}_D\cdot\boldsymbol{n} + \tau^p(p-\hat{p}) & \text{on } \partial\Omega_e\cap\Gamma_D, \\ \widehat{\boldsymbol{u}}\cdot\boldsymbol{n} + \tau^p(p-\hat{p}) & \text{elsewhere} \end{cases} \tag{15c}$$

where τ^p is a newly introduced stabilization coefficient defined to control the compressibility effect due to the relaxation of the continuity equation. A numerical study of its influence will be presented in Section 6.1.1.

It is worth recalling that the choice of the stabilization coefficients $\boldsymbol{\tau}^d$ and $\boldsymbol{\tau}^a$ is known to have a significant role in guaranteeing the well-posedness and optimal convergence of the method, as extensively studied in the HDG [19, 22, 25, 28, 30, 35, 39] and FCFV [8, 9, 12, 16, 17] literature. In this work, the stabilization of the viscous flux is defined as

$$\boldsymbol{\tau}^d := \beta\nu\mathbf{I}_{\mathrm{n_{sd}}} \tag{16}$$

where β is a scalar parameter ranging between 5 and 10 in all the examples presented in Section 6. The effect of the choice of this coefficient on the robustness of the FCFV method has been

extensively investigated in the literature by means of numerical experiments [8, 12, 14, 16, 17].

For the convective term, FCFV stabilizations inspired by classic Riemann solvers have been derived for compressible [12] and incompressible [14] flows, building on the seminal work by Toro [40] and on the unified approach devised for HDG [28]. In this work, Lax-Friedrichs (LF) and Harten-Lax-van Leer (HLL) convective stabilizations are considered, employing the definitions [14]

$$\boldsymbol{\tau}^a_{\mathrm{LF}} := \max\{2|\widehat{\boldsymbol{u}}\cdot\boldsymbol{n}|,\xi\}\mathbf{I}_{\mathrm{n_{sd}}} \tag{17a}$$

$$\boldsymbol{\tau}^a_{\mathrm{HLL}} := \max\{2(\widehat{\boldsymbol{u}}\cdot\boldsymbol{n}),\xi\}\mathbf{I}_{\mathrm{n_{sd}}} \tag{17b}$$

where $\xi = 5\times 10^{-2}$ is a scalar cut-off parameter.

Similarly, the trace of the boundary operator $\boldsymbol{B}$ needs to account for the conditions on the Neumann and symmetry boundaries, namely,

$$\widehat{\boldsymbol{B}}(\boldsymbol{L},\boldsymbol{u},\widehat{\boldsymbol{u}},\hat{p}) := \begin{cases} \hat{p}\boldsymbol{n} + \nu\boldsymbol{L}\boldsymbol{n} + \boldsymbol{\tau}^d(\boldsymbol{u}-\widehat{\boldsymbol{u}}) + \boldsymbol{g} & \text{on } \Gamma_N, \\ \left\{ \begin{array}{l} \boldsymbol{t}_k\cdot\left[\nu\boldsymbol{L}\boldsymbol{n} + \boldsymbol{\tau}^d(\boldsymbol{u}-\widehat{\boldsymbol{u}})\right] \\ \widehat{\boldsymbol{u}}\cdot\boldsymbol{n} \end{array} \right\} & \text{on } \Gamma_S, \\ & \text{for } k = 1,\ldots,\mathrm{n_{sd}}-1. \end{cases} \tag{18}$$

3.5 | Integral Forms of the Hybrid Pressure FCFV Method

The integral forms of the FCFV method with hybrid pressure are obtained after inserting the numerical fluxes (15) into the local, see (13), and global, see (14), problems. It follows that $(\boldsymbol{L},\boldsymbol{u},p)$ are first determined in each cell Ω_e as a function of $(\widehat{\boldsymbol{u}},\hat{p})$ by solving the following set of $\mathrm{n_{el}}$ independent local problems

$$\begin{cases} -\int_{\Omega_e}\boldsymbol{L}\,d\Omega = \int_{\partial\Omega_e\cap\Gamma_D}\left(\boldsymbol{u}_D\otimes\boldsymbol{n} + \boldsymbol{n}\otimes\boldsymbol{u}_D - \frac{2}{3}(\boldsymbol{u}_D\cdot\boldsymbol{n})\mathbf{I}_{\mathrm{n_{sd}}}\right)d\Gamma \\ \qquad\qquad + \int_{\partial\Omega_e\setminus\Gamma_D}\left(\widehat{\boldsymbol{u}}\otimes\boldsymbol{n} + \boldsymbol{n}\otimes\widehat{\boldsymbol{u}} - \frac{2}{3}(\widehat{\boldsymbol{u}}\cdot\boldsymbol{n})\mathbf{I}_{\mathrm{n_{sd}}}\right)d\Gamma, \\ \int_{\partial\Omega_e}\boldsymbol{\tau}\boldsymbol{u}\,d\Gamma = \int_{\Omega_e}\boldsymbol{s}\,d\Omega + \int_{\partial\Omega_e\cap\Gamma_D}(\boldsymbol{\tau}-(\boldsymbol{u}_D\cdot\boldsymbol{n})\mathbf{I}_{\mathrm{n_{sd}}})\boldsymbol{u}_D\,d\Gamma \\ \qquad\qquad + \int_{\partial\Omega_e\setminus\Gamma_D}(\boldsymbol{\tau}-(\widehat{\boldsymbol{u}}\cdot\boldsymbol{n})\mathbf{I}_{\mathrm{n_{sd}}})\widehat{\boldsymbol{u}}\,d\Gamma - \int_{\partial\Omega_e}\hat{p}\boldsymbol{n}\,d\Gamma, \\ -\int_{\partial\Omega_e}\tau^p p\,d\Gamma = \int_{\partial\Omega_e\cap\Gamma_D}\boldsymbol{u}_D\cdot\boldsymbol{n}\,d\Gamma + \int_{\partial\Omega_e\setminus\Gamma_D}\widehat{\boldsymbol{u}}\cdot\boldsymbol{n}\,d\Gamma - \int_{\partial\Omega_e}\tau^p\hat{p}\,d\Gamma \end{cases} \tag{19a}$$

where $\boldsymbol{\tau} = \boldsymbol{\tau}^d + \boldsymbol{\tau}^a$. Similarly, the global problem to determine the velocity $\widehat{\boldsymbol{u}}$ and pressure $\hat{p}$ on the mesh faces is given by

$$\begin{cases} \sum_{e=1}^{\mathrm{n_{el}}}\left\{\int_{\partial\Omega_e\setminus\partial\Omega}\nu\boldsymbol{L}\boldsymbol{n}\,d\Gamma + \int_{\partial\Omega_e\setminus\partial\Omega}\boldsymbol{\tau}\boldsymbol{u}\,d\Gamma \right. \\ \qquad \left. -\int_{\partial\Omega_e\setminus\partial\Omega}\boldsymbol{\tau}\,\widehat{\boldsymbol{u}}\,d\Gamma + \int_{\partial\Omega_e\cap\partial\Omega\setminus\Gamma_D}\widehat{\boldsymbol{B}}(\boldsymbol{L},\boldsymbol{u},\widehat{\boldsymbol{u}},\hat{p})\,d\Gamma\right\} = \boldsymbol{0}, \\ \sum_{e=1}^{\mathrm{n_{el}}}\left\{\int_{\partial\Omega_e}\tau^p p\,d\Gamma - \int_{\partial\Omega_e}\tau^p\hat{p}\,d\Gamma\right\} = 0 \end{cases} \tag{19b}$$

where the cell-by-cell expressions of $\boldsymbol{L}$, $\boldsymbol{u}$, and p are determined from Equation (19a). The corresponding local and global problems for the Stokes equations are reported in Appendix B.

Remark 4. Two observations are important to derive the first equation of (19b). As in standard HDG and FCFV methods [14, 30], the uniqueness of $\widehat{\boldsymbol{u}}$ on the faces of the internal skeleton Γ yields the cancellation of the convective part of the physical flux, hence

$$\sum_{e=1}^{\mathrm{n_{el}}}\int_{\partial\Omega_e\setminus\partial\Omega}(\boldsymbol{\tau}-(\widehat{\boldsymbol{u}}\cdot\boldsymbol{n})\mathbf{I}_{\mathrm{n_{sd}}})\widehat{\boldsymbol{u}}\,d\Gamma = \sum_{e=1}^{\mathrm{n_{el}}}\int_{\partial\Omega_e\setminus\partial\Omega}\boldsymbol{\tau}\,\widehat{\boldsymbol{u}}\,d\Gamma \tag{20a}$$

Following a similar reasoning, also the second term in Equation (14a) vanishes due to the uniqueness of the hybrid pressure on Γ, i.e.,

$$\int_{\partial\Omega_e\setminus\partial\Omega}\hat{p}\boldsymbol{n}\,d\Gamma = 0 \tag{20b}$$

4 | Hybrid Pressure FCFV Discretization

Let $\mathcal{A}_e := \{1,\ldots,\mathrm{n^e_{fa}}\}$ denote the set of indices for all faces of cell Ω_e. The sets $\mathcal{I}_e := \{j\in\mathcal{A}_e \mid \Gamma_{e,j}\cap\partial\Omega = \emptyset\}$ and $\mathcal{E}_e := \{j\in\mathcal{A}_e \mid \Gamma_{e,j}\cap\partial\Omega \neq \emptyset\}$ represent the set of indices for the cell faces interior to the domain and on the boundary, respectively. In addition, $\mathcal{D}_e := \{j\in\mathcal{A}_e \mid \Gamma_{e,j}\cap\Gamma_D \neq \emptyset\}$, $\mathcal{N}_e := \{j\in\mathcal{A}_e \mid \Gamma_{e,j}\cap\Gamma_N \neq \emptyset\}$, and $\mathcal{S}_e := \{j\in\mathcal{A}_e \mid \Gamma_{e,j}\cap\Gamma_S \neq \emptyset\}$ denote the sets of indices for the cell faces on the Dirichlet, Neumann, and symmetry boundaries. To simplify the presentation, the sets $\mathcal{B}_e := \mathcal{A}_e\setminus\mathcal{D}_e$ and $\mathcal{C}_e := \mathcal{E}_e\setminus\mathcal{D}_e$ are also introduced to identify the sets of indices for all cell faces not on a Dirichlet boundary and for all cell faces on any portion of the external boundary, excluding the Dirichlet one. Moreover, recall the definition of the indicator function of a generic set $\mathcal{Z}$ as

$$\chi_{\mathcal{Z}}(i) = \begin{cases} 1 & \text{if } i\in\mathcal{Z}, \\ 0 & \text{otherwise} \end{cases} \tag{21}$$

The discrete form of the FCFV method with hybrid pressure is obtained by describing the cell variables $(\boldsymbol{L},\boldsymbol{u},p)$ using a piecewise constant approximation in each cell and the hybrid variables $(\widehat{\boldsymbol{u}},\hat{p})$ with a constant approximation on each cell face. The corresponding values of the cell variables in Ω_e are denoted by $\mathbf{L}_e$, $\mathbf{u}_e$, and p_e, whereas the hybrid variables on the j-th face $\Gamma_{e,j}$ are denoted by $\hat{\mathbf{u}}_j$ and $\hat{\mathrm{p}}_j$. In addition, $\mathbf{u}_{D,j}$ and $\mathbf{g}_j$ represent the discretizations of the Dirichlet and Neumann data $\boldsymbol{u}_D$ and $\boldsymbol{g}$, respectively, at the barycentre of face $\Gamma_{e,j}$, whereas $\mathbf{s}_e$ is the discretization of the body force $\boldsymbol{s}$ at the centroid of Ω_e. Similarly, $\mathbf{n}_j$ and $\mathbf{t}_{k,j}$ denote the normal vector $\boldsymbol{n}$, and the tangent vector $\boldsymbol{t}_k$ at the barycentre of face $\Gamma_{e,j}$. Finally, integrals in the cells and on the faces are performed using one quadrature point.

Upon discretization, the residuals of the local problem for each cell Ω_e, $e = 1,\ldots,\mathrm{n_{el}}$ are given by

$$\begin{cases} \mathbf{R}_{e,L} := |\Omega_e|\mathbf{L}_e + \sum_{j\in\mathcal{D}_e}|\Gamma_{e,j}|\left(\mathbf{u}_{D,j}\mathbf{n}_j^T + \mathbf{n}_j\mathbf{u}_{D,j}^T - \frac{2}{3}(\mathbf{n}_j^T\mathbf{u}_{D,j})\mathbf{I}_{\mathrm{n_{sd}}}\right) \\ \qquad + \sum_{j\in\mathcal{B}_e}|\Gamma_{e,j}|\left(\hat{\mathbf{u}}_j\mathbf{n}_j^T + \mathbf{n}_j\hat{\mathbf{u}}_j^T - \frac{2}{3}(\mathbf{n}_j^T\hat{\mathbf{u}}_j)\mathbf{I}_{\mathrm{n_{sd}}}\right), \\ \mathbf{R}_{e,u} := \sum_{j\in\mathcal{A}_e}|\Gamma_{e,j}|\boldsymbol{\tau}_j\mathbf{u}_e - |\Omega_e|\mathbf{s}_e - \sum_{j\in\mathcal{D}_e}|\Gamma_{e,j}|\left(\boldsymbol{\tau}_j - (\mathbf{n}_j^T\mathbf{u}_{D,j})\mathbf{I}_{\mathrm{n_{sd}}}\right)\mathbf{u}_{D,j} \\ \qquad - \sum_{j\in\mathcal{B}_e}|\Gamma_{e,j}|\left(\boldsymbol{\tau}_j - (\mathbf{n}_j^T\hat{\mathbf{u}}_j)\mathbf{I}_{\mathrm{n_{sd}}}\right)\hat{\mathbf{u}}_j + \sum_{j\in\mathcal{A}_e}|\Gamma_{e,j}|\hat{\mathrm{p}}_j\mathbf{n}_j, \\ \mathbf{R}_{e,p} := \sum_{j\in\mathcal{A}_e}|\Gamma_{e,j}|\tau_j^p\mathrm{p}_e + \sum_{j\in\mathcal{D}_e}|\Gamma_{e,j}|\mathbf{n}_j^T\mathbf{u}_{D,j} + \sum_{j\in\mathcal{B}_e}|\Gamma_{e,j}|\mathbf{n}_j^T\hat{\mathbf{u}}_j \\ \qquad - \sum_{j\in\mathcal{A}_e}|\Gamma_{e,j}|\tau_j^p\hat{\mathrm{p}}_j \end{cases} \tag{22a}$$

where $|\Omega_e|$ is the area (in 2D) or volume (in 3D) of cell Ω_e and $|\Gamma_{e,j}|$ is the length (respectively, area) of the edge (respectively, face) $\Gamma_{e,j}$ in 2D (respectively, 3D). Moreover, the stabilization coefficients $\boldsymbol{\tau}_j$ and τ_j^p are all evaluated at the barycentre of the corresponding faces.

The residuals of the global problem are to be computed on the mesh faces $\Gamma_{e,i}$, assembling the contributions of cell Ω_e, namely,

$$\begin{cases} \mathbf{R}_{e,i,\hat{u}} := |\Gamma_{e,i}|\left\{\left(\nu \mathbf{L}_e \mathbf{n}_i + \boldsymbol{\tau}_i \mathbf{u}_e - \boldsymbol{\tau}_i\, \hat{\mathbf{u}}_i\right)\chi_{\mathcal{I}_e}(i) + \hat{\mathbf{B}}_i \chi_{\mathcal{C}_e}(i)\right\}, & \text{for all } i \in \mathcal{B}_e, \\ \mathbf{R}_{e,i,\hat{p}} := |\Gamma_{e,i}|\tau_i^p(\mathrm{p}_e - \hat{\mathrm{p}}_i), & \text{for all } i \in \mathcal{A}_e, \end{cases} \tag{22b}$$

where the expression of the discrete boundary operator for the hybrid pressure formulation on face $\Gamma_{e,i}$ is

$$\begin{aligned} \hat{\mathbf{B}}_i &:= \hat{\mathbf{B}}_i(\mathbf{L}_e, \mathbf{u}_e, \hat{\mathbf{u}}_i, \hat{\mathrm{p}}_i, \boldsymbol{\tau}_i^d) \\ &= \begin{cases} \hat{\mathrm{p}}_i \mathbf{n}_i + \nu \mathbf{L}_e \mathbf{n}_i + \boldsymbol{\tau}_i^d(\mathbf{u}_e - \hat{\mathbf{u}}_i) + \mathbf{g}_i & \text{for } i \in \mathcal{N}_e, \\ \left\{ \begin{array}{l} \mathbf{t}_{k,i}^T\left[\nu \mathbf{L}_e \mathbf{n}_i + \boldsymbol{\tau}_i^d(\mathbf{u}_e - \hat{\mathbf{u}}_i)\right] \\ \mathbf{n}_i^T \hat{\mathbf{u}}_i \end{array} \right\} & \text{for } i \in \mathcal{S}_e, \text{ and} \\ & \text{for } k = 1, \ldots, \mathrm{n_{sd}} - 1 \end{cases} \end{aligned} \tag{23}$$

The resulting FCFV discrete problem with hybrid pressure involves the solution of the nonlinear system of equations

$$\mathbf{R}(\mathbf{L}, \mathbf{u}, \mathbf{p}, \hat{\mathbf{u}}, \hat{\mathbf{p}}) = \mathbf{0} \tag{24}$$

obtained by assembling the contributions

$$\mathbf{R}_{e,i} := \begin{Bmatrix} \mathbf{R}_{e,L}(\mathbf{L}_e, \hat{\mathbf{u}}) \\ \mathbf{R}_{e,u}(\mathbf{u}_e, \hat{\mathbf{u}}, \hat{\mathbf{p}}) \\ \mathbf{R}_{e,p}(\mathrm{p}_e, \hat{\mathbf{u}}, \hat{\mathbf{p}}) \\ \mathbf{R}_{e,i,\hat{u}}(\mathbf{L}_e, \mathbf{u}_e, \hat{\mathbf{u}}, \hat{\mathbf{p}})\chi_{\mathcal{B}_e}(i) \\ \mathbf{R}_{e,i,\hat{p}}(\mathrm{p}_e, \hat{\mathbf{p}}) \end{Bmatrix} \tag{25}$$

for $e = 1, \ldots, \mathrm{n_{el}}$ and for $i \in \mathcal{A}_e$.

Remark 5. From a practical viewpoint, the first equation in Equation (22a) is vectorized by means of Voigt notation to impose the symmetry of the mixed variable pointwise. Similarly, Voigt notation is employed to rewrite the terms of the first equation in Equation (22b) involving $\mathbf{L}_e$ to efficiently compute the contraction of the deviatoric strain rate tensor with the normal and tangent vectors by means of standard matrix-vector products. A description of the corresponding implementation details is reported in Appendix A.

4.1 | Newton-Raphson Method for the Incompressible Navier-Stokes Equations

To solve the nonlinear problem (24), the Newton-Raphson method is employed. It is worth noticing that the stabilization tensor $\boldsymbol{\tau}^a$ depends upon the unknown hybrid velocity, see (17). To simplify the linearization of the residuals, at each iteration m of the nonlinear solver, the stabilization tensors are evaluated at iteration $m-1$. While this noticeably simplifies the implementation of the algorithm, numerical experiments not reported here for brevity have shown that it does not affect the stability and convergence of the method. Indeed, since the residuals at iteration m are evaluated using the stabilization with the last computed approximation, the Jacobian matrix obtained by fixing $\boldsymbol{\tau}^a$ at iteration $m-1$ is consistent, and quadratic convergence is observed in all cases. This behavior confirms the results previously observed for the closely related FCFV method for laminar incompressible Navier-Stokes equations [14]. It is worth noticing that the solution of a pseudo-transient problem, performed in the aforementioned reference to guarantee convergence of the Newton-Raphson algorithm for turbulent flows, is not required in the present work. Nonetheless, pseudo-time marching is expected to accelerate convergence also for the hybrid pressure formulation in the presence of stronger nonlinearities, for instance, in the turbulent regime, but this lies beyond the scope of this contribution.

At each iteration m of the Newton-Raphson algorithm, the linear system to be solved is

$$\begin{bmatrix} \mathbf{T}_{UU} & \mathbf{T}_{U\Lambda} \\ \mathbf{T}_{\Lambda U} & \mathbf{T}_{\Lambda\Lambda} \end{bmatrix}^m \begin{Bmatrix} \Delta\mathbf{U} \\ \Delta\boldsymbol{\Lambda} \end{Bmatrix}^m = -\begin{Bmatrix} \mathbf{R}_U \\ \mathbf{R}_\Lambda \end{Bmatrix}^m \tag{26}$$

where the residuals of the local and global problems, respectively, are

$$\mathbf{R}_U := \begin{Bmatrix} \mathbf{R}_L \\ \mathbf{R}_u \\ \mathbf{R}_p \end{Bmatrix}, \qquad \mathbf{R}_\Lambda := \begin{Bmatrix} \mathbf{R}_{\hat{u}} \\ \mathbf{R}_{\hat{p}} \end{Bmatrix} \tag{27a}$$

the block matrices are defined as

$$\begin{aligned} \mathbf{T}_{UU} &:= \begin{bmatrix} \mathbf{T}_{LL} & \mathbf{0} & \mathbf{0} \\ \mathbf{0} & \mathbf{T}_{uu} & \mathbf{0} \\ \mathbf{0} & \mathbf{0} & \mathbf{T}_{pp} \end{bmatrix}, \qquad \mathbf{T}_{U\Lambda} := \begin{bmatrix} \mathbf{T}_{L\hat{u}} & \mathbf{0} \\ \mathbf{T}_{u\hat{u}} & \mathbf{T}_{u\hat{p}} \\ \mathbf{T}_{p\hat{u}} & \mathbf{T}_{p\hat{p}} \end{bmatrix} \\ \mathbf{T}_{\Lambda U} &:= \begin{bmatrix} \mathbf{T}_{\hat{u}L} & \mathbf{T}_{\hat{u}u} & \mathbf{0} \\ \mathbf{0} & \mathbf{0} & \mathbf{T}_{\hat{p}p} \end{bmatrix}, \qquad \mathbf{T}_{\Lambda\Lambda} := \begin{bmatrix} \mathbf{T}_{\hat{u}\hat{u}} & \mathbf{T}_{\hat{u}\hat{p}} \\ \mathbf{0} & \mathbf{T}_{\hat{p}\hat{p}} \end{bmatrix} \end{aligned} \tag{27b}$$

with $\mathbf{T}_{ab}$ being the tangent matrix obtained from the contribution $(\mathbf{T}_{ab})_{e,i} := \partial \mathbf{R}_{e,i,a}/\partial b$, whereas the solution increments from iteration m to iteration $m+1$ are denoted by $\Delta\circledcirc^m = \circledcirc^{m+1} - \circledcirc^m$, with

$$\mathbf{U} := \begin{Bmatrix} \mathbf{L} \\ \mathbf{u} \\ \mathbf{p} \end{Bmatrix}, \qquad \boldsymbol{\Lambda} := \begin{Bmatrix} \hat{\mathbf{u}} \\ \hat{\mathbf{p}} \end{Bmatrix} \tag{27c}$$

The structure of the resulting system (26) allows for the cell unknowns in $\mathbf{U}$ to be eliminated by computing the Schur complement of the problem, thus leading to a smaller global system involving only the face unknowns $\boldsymbol{\Lambda}$, namely,

$$\mathbb{K}^m \Delta\boldsymbol{\Lambda}^m = \mathbb{F}^m \tag{28}$$

with $\mathbb{K} := \mathbf{T}_{\Lambda\Lambda} - \mathbf{T}_{\Lambda U}\mathbf{T}_{UU}^{-1}\mathbf{T}_{U\Lambda}$ and $\mathbb{F} := -\mathbf{R}_\Lambda + \mathbf{T}_{\Lambda U}\mathbf{T}_{UU}^{-1}\mathbf{R}_U$. Note that the inverse of matrix $\mathbf{T}_{UU}$ can be easily computed analytically. Indeed, stemming from the choice of applying the divergence theorem as discussed in Section 3.2, $\mathbf{T}_{UU}$ features a block-diagonal structure.

Remark 6. Contrary to the FCFV formulation [8, 14], the matrix $\mathbb{K}$ in Equation (28) does not feature a saddle point

structure. This follows from the introduction of the hybrid pressure unknown in the formulation and, consequently, from the presence of a non-zero block $\mathbf{T}_{\hat{p}\hat{p}}$ in the matrix $\mathbf{T}_{\Lambda\Lambda}$. Section 5 further discusses the structure and the properties of the resulting matrix $\mathbb{K}$, whereas its detailed expression for the linear case (see Equation (B5)) and the derivation of the hybrid pressure formulation for the Stokes equations are reported in Appendix B.

Upon solving (28), the cell unknowns $\mathbf{U}$ can be retrieved by computing, independently in each cell,

$$\mathbf{T}_{UU}^{m}\Delta\mathbf{U}^{m} = -\mathbf{R}_{U}^{m} - \mathbf{T}_{U\Lambda}^{m}\Delta\mathbf{\Lambda}^{m} \tag{29}$$

It is worth noticing that, given the block-diagonal structure of $\mathbf{T}_{UU}$, the local variables $\mathbf{L}$, $\mathbf{u}$, and $\mathbf{p}$ are decoupled from one another, and the computation of Equation (29) is computationally inexpensive.

Remark 7. The computation of the reduced matrix $\mathbb{K}$ and vector $\mathbb{F}$ in Equation (28) corresponds to the hybridization step described in Section 3.2 and is the algebraic counterpart of the solution of the local problem (19a). This strategy is equivalent to the well-known static condensation and hybridization procedures commonly performed for high-order finite element approximations [20, 21, 41, 42].

5 | Computational Aspects

The implementation of the hybrid pressure FCFV solver features three stages: (i) constructing matrix $\mathbb{K}$ and vector $\mathbb{F}$ at each iteration of the Newton-Raphson algorithm; (ii) solving Equation (28) to determine the face variables; (iii) retrieving the cell variables by means of (29). As discussed in Section 4.1, the first and last steps are computationally inexpensive since (i) can be performed analytically and (iii) exploits the block-diagonal structure of matrix $\mathbf{T}_{UU}$ to decouple the computation. Hence, the main cost of the hybrid pressure FCFV method lies in the solution of the global problem (28) in step (ii). The simulations of the Navier-Stokes cases in Section 6 are obtained with a Fortran 90 implementation of the method, relying on PETSc [43] for direct linear solvers.

In this context, the introduction of the face unknowns for pressure represents a major difference with respect to the FCFV method [8, 14], resulting in larger systems to be solved. Table 1 presents an estimate of the expected number of degrees of freedom of the hybrid pressure formulation with respect to the FCFV approach [8], neglecting the boundary unknowns. On the one hand, the hybrid pressure formulation accounts for one degree of freedom for each component of the velocity and an additional one for pressure on each face, yielding a total of $(\mathtt{n_{sd}}+1)\mathtt{n_{fa}}$ unknowns, $\mathtt{n_{fa}}$ being the number of mesh faces. On the other hand, the FCFV approach also features one face unknown per component of velocity, whereas pressure is discretized in each of the $\mathtt{n_{el}}$ cells, leading to a system of dimension $\mathtt{n_{sd}n_{fa}}+\mathtt{n_{el}}$. Hence, using simplicial meshes, less than 15% extra degrees of freedom are required to construct the hybrid pressure system with respect to the FCFV one.

The introduction of the face unknowns for pressure is also responsible for a significant change in the definition of the matrix of the global problem. Figure 2 reports the sparsity pattern of the global system obtained using the hybrid pressure formulation and the FCFV method. For the sake of simplicity, a linear case is considered by neglecting the convection term in the Navier-Stokes equations. The resulting problem under analysis is a two-dimensional Stokes flow in a unit square domain, discretized by means of a structured mesh consisting of 16×16 quadrilateral cells. The sparsity pattern is presented without any renumbering of the degrees of freedom to showcase the block structure of the problem. Of course, before solving the system, a reordering procedure should be applied to reduce the bandwidth of the matrix.

TABLE 1 | Comparison of the expected number of degrees of freedom for the hybrid pressure formulation and the FCFV method using meshes of different cell types.

				Hybrid pressure	**FCFV**
Cell type	**Vertices**	**Cells**	**Faces**	$\mathtt{n_{dof}}$	$\mathtt{n_{dof}}$
Quadrilaterals	n	n	$2n$	$6n$	$5n$
Triangles	n	$2n$	$3n$	$9n$	$8n$
Tetrahedra	n	$5n$	$10n$	$40n$	$35n$
Hexahedra	n	n	$3n$	$12n$	$10n$
Prisms	n	$2n$	$5n$	$20n$	$17n$
Pyramids	n	$8n/5$	$4n$	$16n$	$68n/5$

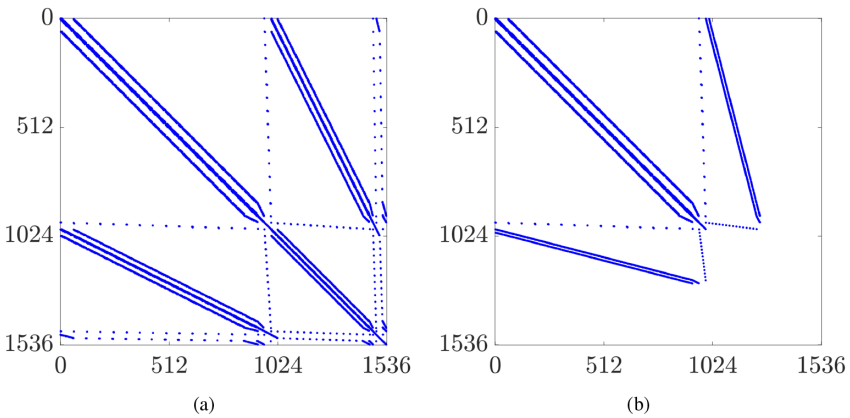

FIGURE 2 | Sparsity pattern of the matrix of the global system of a Stokes flow computed using (a) hybrid pressure formulation and (b) FCFV method.

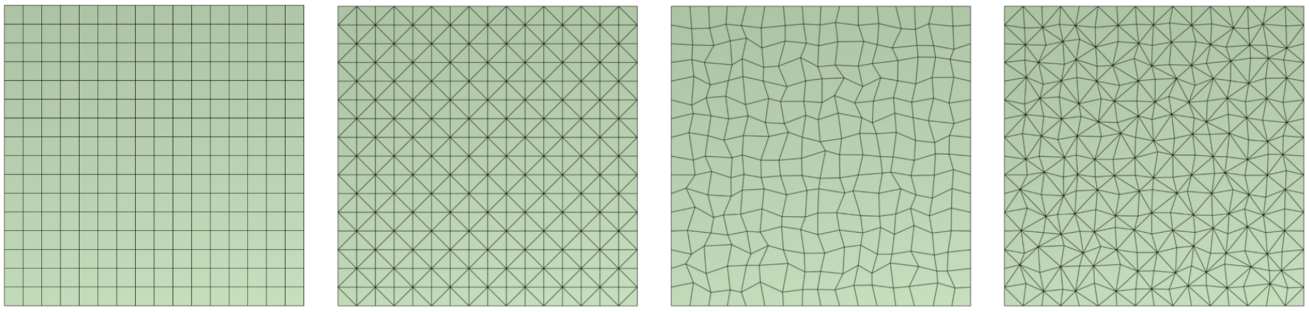

(a) (b) (c) (d)

FIGURE 3 | Computational meshes of quadrilateral and triangular cells used to study the spectrum of the global matrix. (a) Regular meshes, (b) Regular meshes, (c) Distorted meshes, and (d) Distorted meshes.

Several aspects of the structure of the hybrid pressure matrix are worth commenting on. Whilst the matrix blocks associated with the face velocities (top left) are comparable in the two approaches, both the off-diagonal terms and the pressure block present significant differences.

The off-diagonal blocks feature a more complex structure than the FCFV ones, as visible in Figure 2a. Indeed, the dependence of both cell unknowns $\boldsymbol{u}$ and p on the face unknowns $\widehat{\boldsymbol{u}}$ and $\hat{p}$, see (19a), is responsible for introducing a stronger coupling between velocity and pressure in the hybrid pressure formulation, instead of $\boldsymbol{u}$ depending exclusively on $\widehat{\boldsymbol{u}}$ (see equation 34b of the FCFV formulation [8]) and the cell pressure being used to enforce incompressibility cell-by-cell (see equation 37b of the FCFV formulation [8]). Moreover, the employment of a pointwise symmetric mixed variable (i.e., $\boldsymbol{L}$ in Equation (7) instead of the scaled gradient of velocity in equation 25 of the FCFV formulation [8]) also introduces additional coupling between hybrid velocity and hybrid pressure via the inter-cell continuity of the momentum flux in Equation (19b).

This additional richness of information is also testified by the larger number of non-zero entries in the resulting system for the hybrid pressure formulation: Whilst the $1,536 \times 1,536$ matrix in Figure 2a features 30,448 non-zero entries, the FCFV matrix depicted in Figure 2b has 10,728 non-null terms over a total of $1,248 \times 1,248$ entries, whereas the number of degrees of freedom of pressure only increased from 256 to 544.

Moreover, it is worth remarking that the hybrid pressure formulation no longer features the saddle point structure present in the FCFV matrix, as commented in Section 4.1. This is a direct consequence of introducing the new variable $\hat{p}$, which yields the matrix block $\mathbf{T}_{\hat{p}\hat{p}}$ in $\mathbf{T}_{\Lambda\Lambda}$ (27b) and the non-zero bottom-right block visible in Figure 2a.

A numerical study of the properties of the spectrum of the global matrix is now presented using the discretization of a Stokes flow defined on a unit square domain. Four meshes are considered, two featuring quadrilateral cells and two consisting of triangles: The quadrilateral meshes consist of 16×16 cells, whereas the meshes of triangular cells are composed of $16 \times 16 \times 2$ triangles. Each set of meshes accounts for *regular* meshes with uniform cell size (Figure 3a,b) and *distorted* meshes in which the coordinates of the internal mesh nodes have been perturbed by means of a random value at most equal to the 30% of the shortest edge emanating from such a node (Figure 3c,d).

Table 2 reports the minimum and maximum eigenvalues of the matrix of the global problem obtained from the hybrid pressure and FCFV discretizations.

Contrary to the FCFV matrix, whose eigenvalues are all real numbers, the results show that the hybrid pressure matrix exhibits a certain number of complex eigenvalues. It is worth noticing that, in all analyzed cases, these eigenvalues represent less than 7% of the total number of eigenvalues. Moreover, the magnitude of the corresponding imaginary parts always ranges between 10^{-6} and 10^{-4}, thus significantly below the accuracy of the mesh under analysis, the corresponding cell size being 0.62×10^{-1}. In addition, whilst the FCFV matrix features a saddle point structure, thus having both positive and negative eigenvalues, the matrix arising from the hybrid pressure formulation only presents negative eigenvalues. Note also that the maximum eigenvalue for the hybrid pressure approach always remains bounded below zero, being almost insensitive to cell type and cell distortion. Hence, the performed numerical studies suggest that the matrix obtained from the hybrid pressure discretization is negative definite, but further theoretical analyses are required to confirm this conclusion. Nonethless, these observations give promising insights on the possibility to develop efficient iterative schemes and preconditioners for the hybrid pressure FCFV method, which lie outside the scope of the present work.

6 | Numerical Results

Four examples are presented in this section to numerically evaluate the properties of the hybrid pressure formulation. First, in Section 6.1, it is shown that the method can be successfully employed to approximate the linear case of Stokes equations, achieving optimal convergence of order one for velocity, pressure, and deviatoric stress tensor, independently of cell type (quadrilaterals/triangles) and cell distortion. Moreover, the capability of the method to guarantee mass conservation, although incompressibility is only enforced in a weak sense, is verified numerically. Then, the method is used to simulate a suite of steady-state incompressible Navier-Stokes flows. The Couette flow (Section 6.2) is employed to assess the convergence properties of

TABLE 2 | Minimum and maximum eigenvalues of the global matrix for a Stokes flow using hybrid pressure formulation and FCFV method.

Mesh type	$\mathcal{R}e(\lambda_{\min})$	$\mathcal{R}e(\lambda_{\max})$	$\mathcal{I}m(\lambda_{\min})$	$\mathcal{I}m(\lambda_{\max})$
		Hybrid pressure		
Regular quadrilaterals	-11.7	-0.16×10^{-3}	-0.34×10^{-5}	0.34×10^{-5}
Distorted quadrilaterals	-13.9	-0.16×10^{-3}	-0.11×10^{-5}	0.11×10^{-5}
Regular triangles	-18.9	-0.17×10^{-3}	-0.65×10^{-6}	0.65×10^{-6}
Distorted triangles	-30.0	-0.17×10^{-3}	-0.24×10^{-4}	0.24×10^{-4}
		FCFV		
Regular quadrilaterals	-7.7	0.40×10^{-2}	0.00	0.00
Distorted quadrilaterals	-10.9	0.49×10^{-2}	0.00	0.00
Regular triangles	-13.5	0.32×10^{-2}	0.00	0.00
Distorted triangles	-22.7	0.50×10^{-2}	0.00	0.00

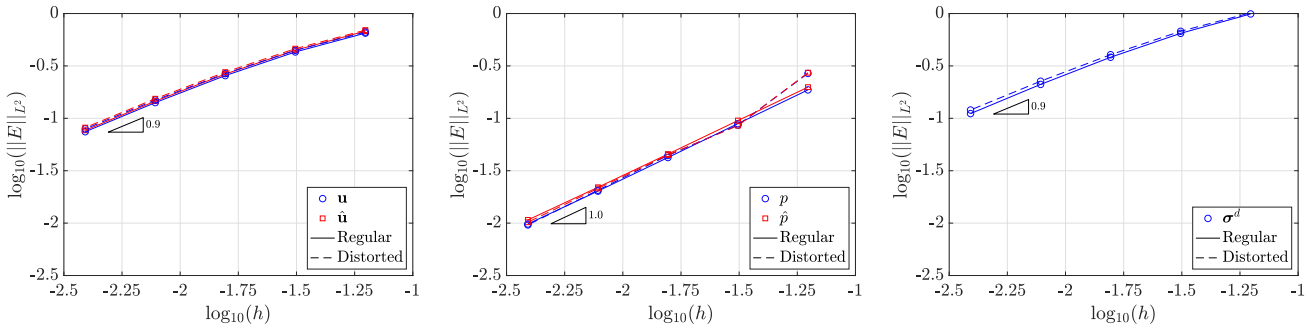

(a) (b) (c)

FIGURE 4 | Synthetic Stokes flow—Mesh convergence of the error of (a) velocity and hybrid velocity, (b) pressure and hybrid pressure, and (c) deviatoric stress tensor, measured in the $\mathcal{L}_2$ norm as a function of the cell size h on meshes of regular and distorted quadrilateral cells.

the method. The lid-driven cavity flow is simulated for different Reynolds numbers in Section 6.3, demonstrating the capability of the method to accurately approximate convection-dominated flows, using different Riemann solvers. Finally, the three-dimensional flow past a sphere confirms the robustness and the accuracy of the approach, also with unstructured meshes of tetrahedra (Section 6.4). Specific attention is devoted to the comparison of the results with reference solutions, when available in the literature, and with the previously published FCFV method [14], showcasing the superior performance of the hybrid pressure formulation in the presence of convective effects.

6.1 | A Synthetic Stokes Flow

In this section, the optimal convergence properties of the method are numerically verified for the Stokes equations using a two-dimensional synthetic problem with viscosity $\nu = 1$. The computational domain is $\Omega = [0,1]^2$ and the boundary $\partial\Omega$ is composed of two disjoint portions, $\Gamma_N := \{(x_1, x_2) \in \mathbb{R}^2 \mid x_2 = 0\}$ and $\Gamma_D := \partial\Omega \setminus \Gamma_N$. Starting from an analytical solution of the flow equations [44], velocity $\boldsymbol{u} = (u_1, u_2)^T$ and pressure are defined as

$$\boldsymbol{u}(x_1,x_2) = \begin{Bmatrix} (1-\cos(2\pi x_1))\sin(2\pi x_2) \\ -\sin(2\pi x_1)(1-\cos(2\pi x_2)) \end{Bmatrix}$$
$$p(x_1,x_2) = \cos(\pi x_1) + \cos(\pi x_2) \tag{30}$$

and they are used to determine the analytical expressions of body force $\boldsymbol{s}$, Dirichlet datum $\boldsymbol{u}_D$, and Neumann condition $\boldsymbol{g}$.

Five structured meshes of quadrilateral cells are employed to estimate the convergence rate of the method. The meshes are uniformly refined and the i-th mesh consists of $(8\times2^i)\times(8\times2^i)$ quadrilateral cells. In addition, the effect of cell distortion on the accuracy of the computations is assessed by displacing the position of each internal mesh node by a random perturbation of up to 30% of the length of the shortest edge sharing the node [8]. The meshes previously displayed in Figure 3a,c, respectively, represent the first level of refinement for regular and distorted meshes of quadrilateral cells.

Setting $\tau^p = 10^{-1}$, Figure 4 displays the relative error, measured in the $\mathcal{L}_2$ norm as a function of the characteristic cell size h, for cell and face velocity (left), cell and face pressure (centre), and

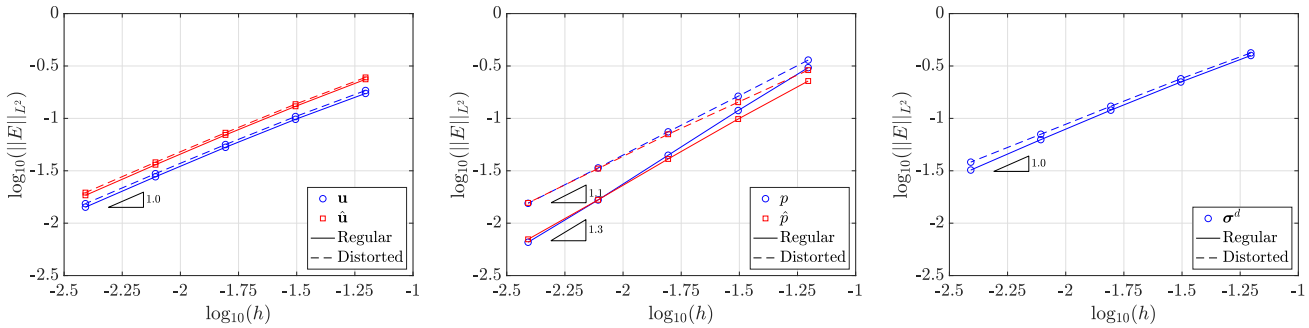

FIGURE 5 | Synthetic Stokes flow—Mesh convergence of the error of (a) velocity and hybrid velocity, (b) pressure and hybrid pressure, and (c) deviatoric stress tensor, measured in the $\mathcal{L}_2$ norm as a function of the cell size h on meshes of regular and distorted triangular cells.

deviatoric stress tensor (right). The results show that, upon mesh refinement, the FCFV method with hybrid pressure achieves the optimal convergence rate of order one for velocity, pressure, and stress tensor. As already observed for the FCFV method [8, 12–14], the convergence rates are preserved even in the presence of distorted cells. Moreover, the error levels achieved on regular and distorted meshes remain practically identical for all variables, showing that the hybrid pressure formulation is less sensitive to cell distortion than traditional CCFV and VCFV methods [6, 7].

The test is repeated using a set of meshes with triangular cells, obtained by splitting each quadrilateral in the above meshes by means of one diagonal. The resulting i-th mesh consists of $(8 \times 2^i) \times (8 \times 2^i) \times 2$ triangles. The first level of refinement of these computational meshes has been presented in Figure 3b,d for regular and distorted cells. The corresponding convergence of the error for cell and face velocity, cell and face pressure, and deviatoric stress tensor is reported in Figure 5. The results confirm the optimal convergence rate of order one and almost identical errors for cell and face velocity and deviatoric stress tensor, on both regular and distorted meshes. Cell and face pressure converge optimally with order one on distorted meshes, whereas, in this problem, they experience superconvergence on regular meshes, achieving order 1.3.

6.1.1 | Influence of the Stabilization Parameter on Mass Conservation

As previously mentioned (see Section 3.4), the hybrid pressure formulation requires the introduction of a new stabilization coefficient in the definition of the mass flux. A sensitivity study is presented to showcase the robustness of the method to the choice of this parameter. Figure 6 displays the $\mathcal{L}_2$ norm of the error for cell and face velocity (left), cell and face pressure (centre), and deviatoric stress tensor (right) as a function of τ^p, for different levels of refinement of the meshes of quadrilateral and triangular cells employed in the previous convergence study.

The accuracy of the approximation of $\boldsymbol{u}$, $\widehat{\boldsymbol{u}}$, and $\boldsymbol{\sigma}^d$ appears to be almost independent of the choice of τ^p, for both quadrilateral and triangular cells, and for any mesh refinement considered. On the contrary, the accuracy of the cell and face pressure is affected by the choice of τ^p, but a common trend can be identified for different meshes and cell types. Given the results in Figure 6, all the simulations in the present work are performed using $\tau^p = 10^{-1}$.

It is worth recalling that, according to the definition of the mass flux (15c), τ^p has a direct influence on the fulfillment of the incompressibility equation. In particular, τ^p can be interpreted as a measure of the compressibility effect introduced by enforcing mass conservation weakly. To assess the accuracy of the hybrid pressure formulation to impose the incompressibility constraint, let us introduce the cell mass flux

$$\mathrm{J}_e := \int_{\partial\Omega_e \setminus \Gamma_D} \widehat{\boldsymbol{u}} \cdot \boldsymbol{n} \, d\Gamma + \int_{\partial\Omega_e \cap \Gamma_D} \boldsymbol{u}_D \cdot \boldsymbol{n} \, d\Gamma \tag{31}$$

Figure 7 displays the maximum norm of the cell mass flux J_e, for different levels of mesh refinement and cell types, when the value of the stabilization coefficient τ^p is modified. Note that while the exact value of J_e is zero for each cell, this quantity serves as a measure of the error in the approximation of the cell's mass flux. Of course, as $\tau^p \to 0$, the approximation of the velocity tends to be perfectly divergence-free and $\mathrm{J}_e \to 0$. On the contrary, for large values of τ^p, the incompressibility constraint is not well enforced, but the error decreases as the mesh is refined.

Nonetheless, the maximum mass flux error, reported in Table 3 for $\tau^p = 10^{-1}$ and different meshes of quadrilateral and triangular cells, is always at least one order of magnitude smaller than the corresponding best approximation error of order h that can be achieved by a given mesh. Hence, although the hybrid pressure formulation only enforces incompressibility in a weak sense, the error introduced in the mass conservation of a given cell is negligible with respect to the spatial discretization error. Moreover, at the global level, upon summing the contributions J_e of all cells Ω_e, $e = 1, \ldots, \mathrm{n_{el}}$, the mass flux error achieves values of order 10^{-12} for all meshes, and the mass conservation equation is thus verified at machine precision. Similar results, not reported here for brevity, were obtained using distorted meshes, with maximum cell mass flux errors ranging from 0.92×10^{-2} to 0.13×10^{-4}.

Additional numerical tests have been performed for the Stokes flow, including the two-dimensional cavity flow and the flow past a sphere in 3D. The results confirmed the previously observed optimal convergence properties of the hybrid pressure formulation, its accuracy using different cell types (quadrilaterals,

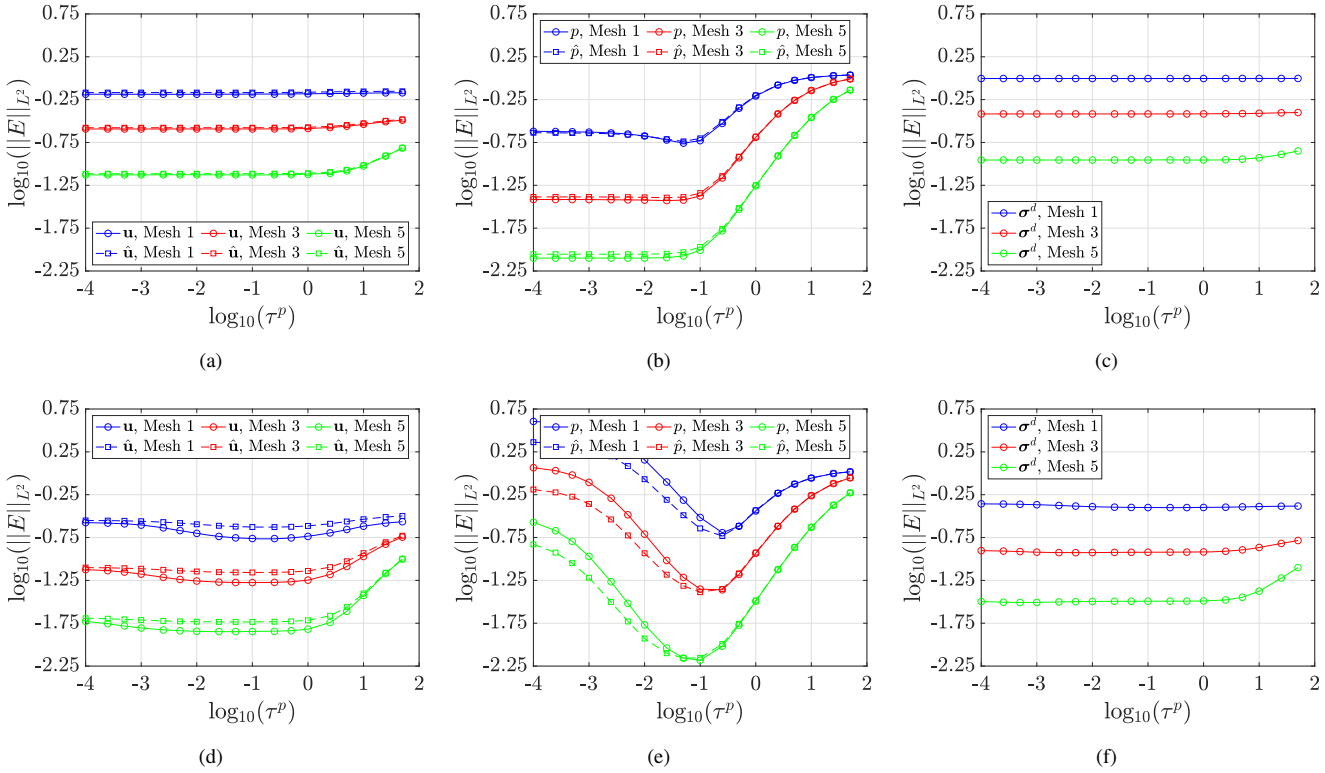

FIGURE 6 | Synthetic Stokes flow—Sensitivity of the error for (a,d) velocity and hybrid velocity, (b,e) pressure and hybrid pressure, and (c,f) deviatoric stress tensor, measured in the $\mathcal{L}_2$ norm as a function of the stabilization coefficient τ^p for different levels of mesh refinement. Top row: Quadrilateral meshes, Bottom row: Triangular meshes.

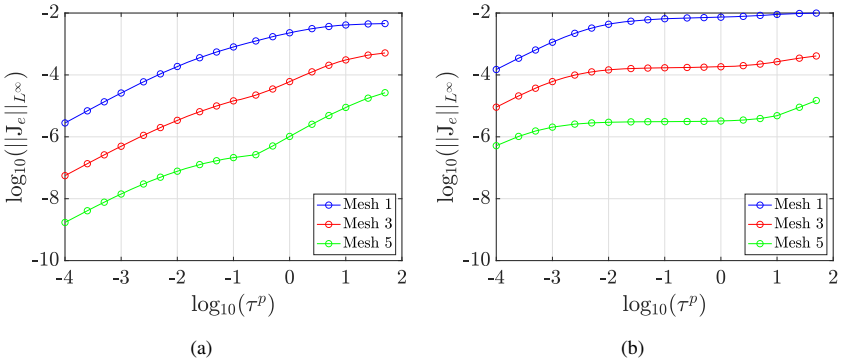

FIGURE 7 | Synthetic Stokes flow—Sensitivity of the cell mass flux J_e, measured in the $\mathcal{L}_\infty$ norm, as a function of the stabilization coefficient τ^p on different levels of mesh refinement of (a) quadrilateral and (b) triangular cells.

TABLE 3 | Synthetic Stokes flow—maximum cell mass flux J_e with $\tau^p = 10^{-1}$ for different levels of refinement of the regular meshes.

Mesh	1	2	3	4	5
h	0.62×10^{-1}	0.31×10^{-1}	0.16×10^{-1}	0.78×10^{-2}	0.39×10^{-2}
Quadrilaterals	0.80×10^{-3}	0.12×10^{-3}	0.14×10^{-4}	0.16×10^{-5}	0.21×10^{-6}
Triangles	0.65×10^{-2}	0.11×10^{-2}	0.17×10^{-3}	0.23×10^{-4}	0.31×10^{-5}

triangles, and tetrahedra), and its robustness in the presence of unstructured, distorted, and stretched meshes. It is worth noticing that all results were comparable with the ones provided by the previously published FCFV method [8], and they are not reported here for brevity. In particular, it was observed that the advantages of one approach over the other were mainly problem-dependent when dealing with the Stokes equations. Hence, the remaining of this work will focus on Navier-Stokes flows to showcase the superiority of the hybrid pressure formulation in the presence of convection phenomena.

6.2 | Navier-Stokes Couette Flow

In this section, the numerical convergence analysis of the hybrid pressure formulation is performed for a two-dimensional incompressible Navier-Stokes flow with an analytical solution. The test case under analysis is the co-axial Couette flow, defined on the computational domain $\Omega := \{(x_1, x_2) \in \mathbb{R}^2 \mid R_i \leq r(x_1, x_2) \leq R_o\}$, with $r := (x_1^2 + x_2^2)^{1/2}$. The setup of the problem represents an annulus centred in $(0, 0)$, with inner and outer radii $R_i = 1$ and $R_o = 2$, respectively, rotating with imposed angular velocities $\omega_i = 0$ and $\omega_o = 0.5$, respectively.

The analytical velocity $\boldsymbol{u} = (u_r, u_\phi)^T$ and pressure, expressed in polar coordinates, are given by

$$\boldsymbol{u}(r) = \left\{ \begin{array}{c} 0 \\ C_1 r + C_2 \frac{1}{r} \end{array} \right\}, \quad p(r) = C_1^2 \frac{r^2}{2} + 2C_1 C_2 \log(r) - \frac{C_2^2}{2r^2} + C \tag{32}$$

with $C_1 := (\omega_o R_o^2 - \omega_i R_i^2)/(R_o^2 - R_i^2)$ and $C_2 := (\omega_i - \omega_o) R_i^2 R_o^2/(R_o^2 - R_i^2)$, whereas C denotes a constant selected to guarantee that the pressure at R_o is equal to 1. Note that the solution pair $(\boldsymbol{u}, p)$ does not depend upon viscosity, and ν is set to 1. Considering $|R_o - R_i|$ as the characteristic length of the problem and setting the magnitude of $\boldsymbol{u}$ at $r = R_o$ as the characteristic velocity, the corresponding value of the Reynolds number is 1.

Setting $\xi = 5 \times 10^{-2}$ in the definition of the HLL convective stabilization (17b), the Newton-Raphson solver is executed with a tolerance of 10^{-10}. A mesh convergence study is performed using structured meshes of regular and distorted, quadrilateral and triangular cells. Figure 8 displays the first level of mesh refinement, featuring 32 subdivisions in the tangential direction and 8 in the radial one. In general, the i-th level of mesh refinement is characterized by $(8 \times 2^i) \times (8 \times 2^i)$ cells [14]. Similarly to the experiments presented in Section 6.1, the effect of cell distortion is evaluated by introducing a random perturbation of the internal mesh nodes.

Figures 9 and 10 display the optimal convergence of the error for cell and face velocity (left), cell and face pressure (centre), and deviatoric stress tensor (right), upon mesh refinement, for quadrilateral and triangular cells. The behavior of the $\mathcal{L}_2$ norm of the relative error confirms the results previously observed in the case of the Stokes flow, with all variables optimally converging with order one, independently of cell type or distortion. It is worth noticing that, given the extremely low value of the Reynolds number, the flow under analysis is similar to a Stokes flow, and no significant accuracy gain is expected in this problem. Indeed, the comparison of the hybrid pressure formulation with the FCFV method [14] shows that the approximations of velocity and deviatoric stress tensor are almost superimposed. Concerning the discretization of p, the hybrid pressure formulation shows slightly increased robustness, achieving approximately the same accuracy using regular and distorted meshes. On the contrary, the FCFV method attains optimal convergence for pressure in both types of grid, but it suffers a slight loss of accuracy due to the distortion of the cells (see Figure 9a,b).

Concerning mass conservation, Figure 11 reports the absolute value of the cell mass flux in logarithmic scale, i.e., $\log_{10} |\mathrm{J}_e|$. The results show that the maximum error in the cell-by-cell mass conservation ranges from 10^{-3} to 0.4×10^{-2} for the first mesh of quadrilateral and triangular cells, respectively. Note that this is significantly below the corresponding best approximation error that can be achieved with these meshes, where $h \simeq 0.4$ for both quadrilaterals and triangles. Moreover, this error consistently decreases when the mesh is refined, achieving values of the order of 10^{-6} on the fourth mesh, while the corresponding mesh size is of order 0.2×10^{-1} for both meshes. It is worth noticing that the distortion of the cells (bottom row of the figure) affects only marginally the error in the cell-wise incompressibility, increasing the maximum error by a moderate factor, always significantly below the best approximation error of the mesh. Finally, the total mass flux obtained by summing the contributions J_e for all mesh cells achieves machine precision independently of the level of mesh refinement, thus confirming the ability of the hybrid pressure formulation to globally preserve the mass in the domain.

6.3 | Navier-Stokes Flow in a Lid-Driven Cavity

The third example presents the flow in a lid-driven cavity at $Re = 1,000$ and $Re = 3,200$. Given the domain $\Omega = [0, 1]^2$, a constant horizontal velocity field $\boldsymbol{u}_D = [1, 0]^T$ is imposed on the top lid, whereas no-slip conditions are enforced on the remaining portions of the boundary. Given the height of the domain as characteristic length and the magnitude of $\boldsymbol{u}_D$ as characteristic velocity, the viscosity ν is set to $1/Re$.

The goal of this test is to evaluate the influence of different choices of convective stabilization on the hybrid pressure

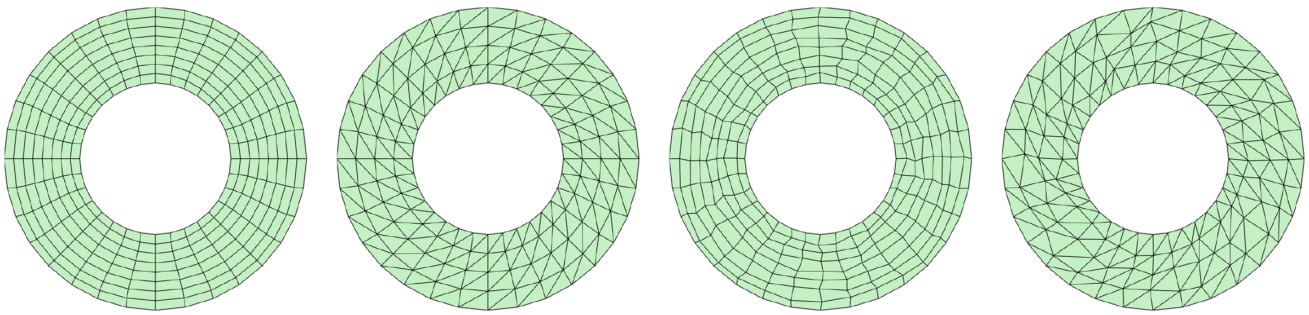

FIGURE 8 | Couette Navier-Stokes flow—First level of refinement of the meshes of quadrilateral and triangular cells. (a) Regular meshes, (b) Regular meshes, (c) Distorted meshes, and (d) Distorted meshes.

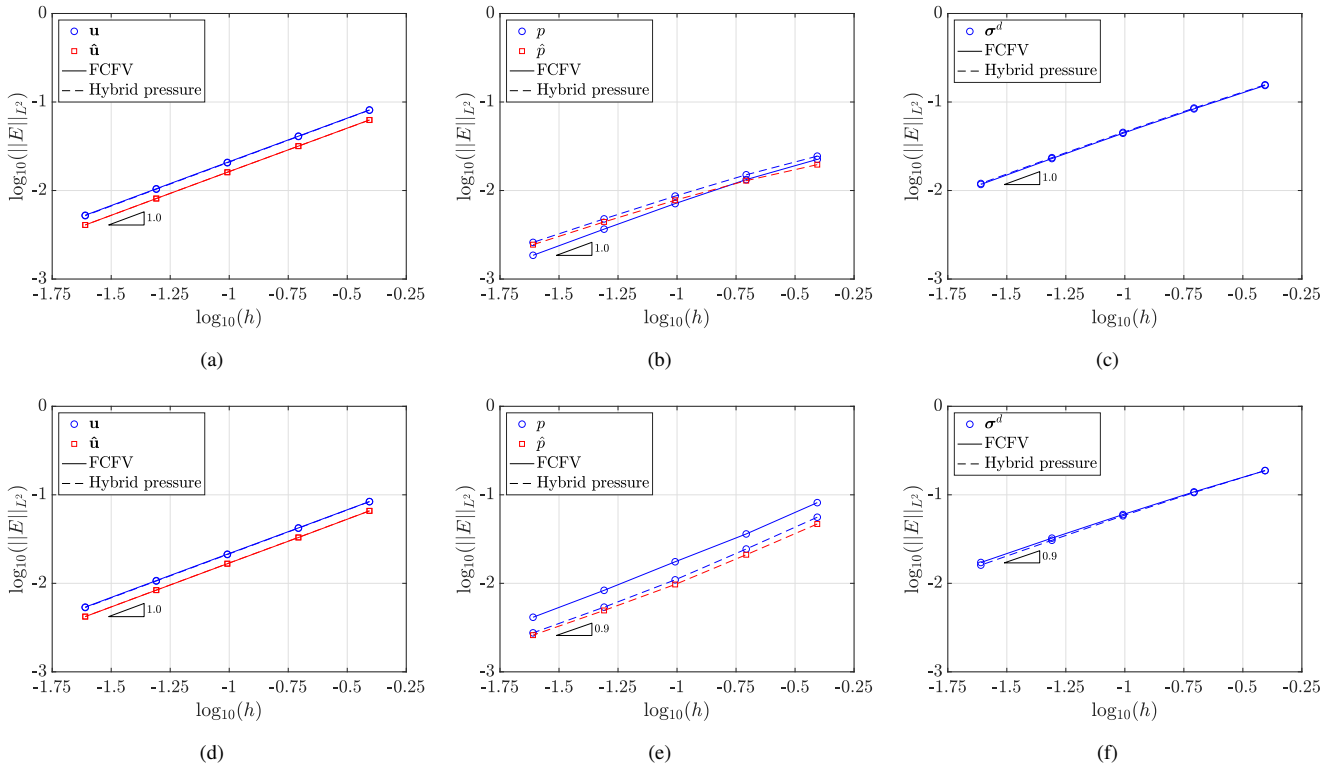

FIGURE 9 | Couette Navier-Stokes flow—Mesh convergence of the error of (a,d) velocity and hybrid velocity, (b,d) pressure and hybrid pressure, and (c,f) deviatoric stress tensor, measured in the $\mathcal{L}_2$ norm as a function of the cell size h on meshes of quadrilateral cells. Top row: Regular meshes, Bottom row: Distorted meshes.

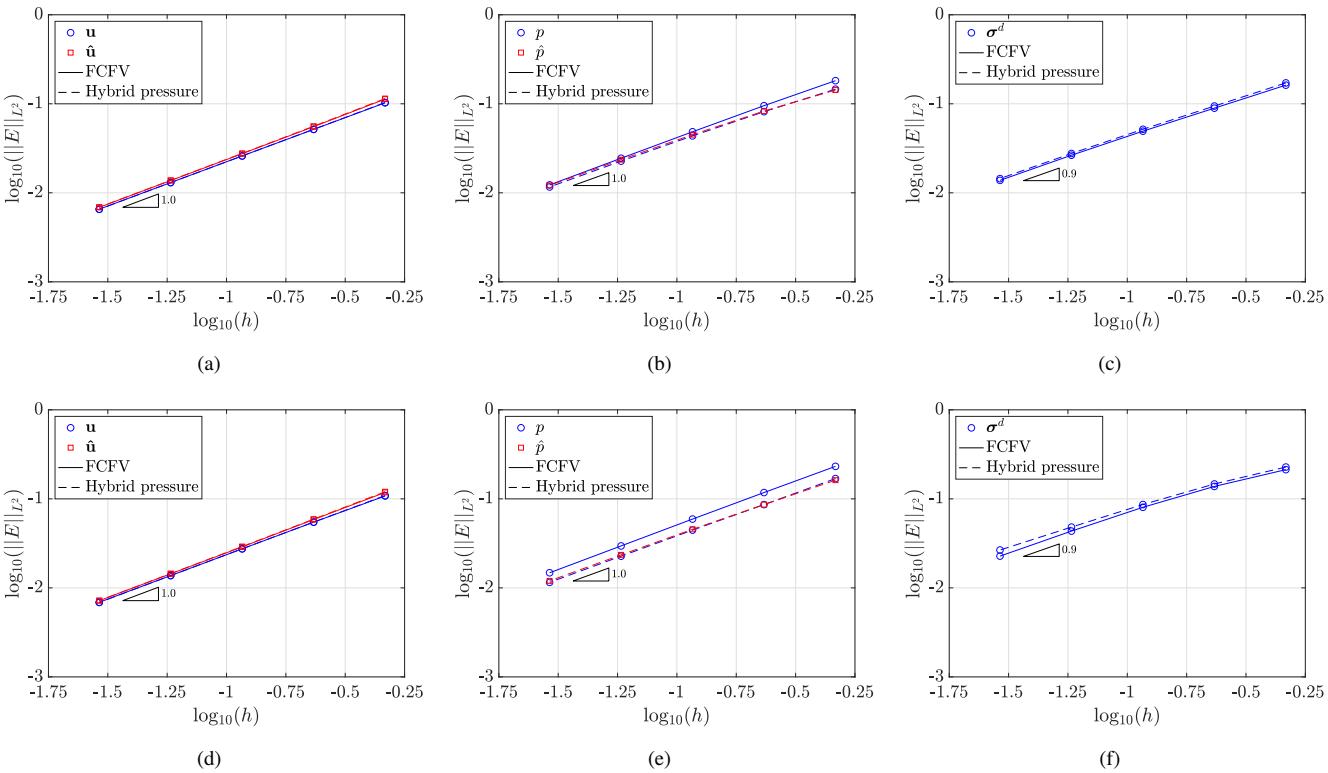

FIGURE 10 | Couette Navier-Stokes flow—Mesh convergence of the error of (a,d) velocity and hybrid velocity, (b,d) pressure and hybrid pressure, and (c,f) deviatoric stress tensor, measured in the $\mathcal{L}_2$ norm as a function of the cell size h on meshes of triangular cells. Top row: Regular meshes, Bottom row: Distorted meshes.

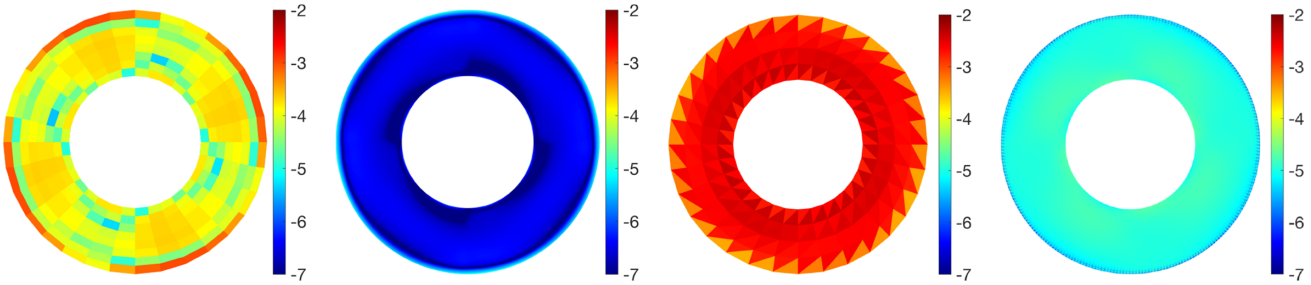

(a) Quadrilaterals - Mesh 1 (b) Quadrilaterals - Mesh 4 (c) Triangles - Mesh 1 (d) Triangles - Mesh 4

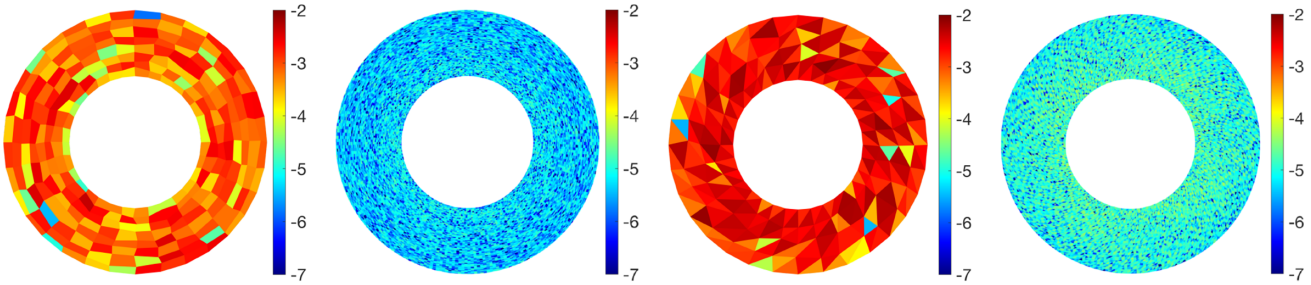

(e) Quadrilaterals - Mesh 1 (f) Quadrilaterals - Mesh 4 (g) Triangles - Mesh 1 (h) Triangles - Mesh 4

FIGURE 11 | Couette Navier-Stokes flow—Cell mass flux $\log_{10}|J_e|$ for the first and fourth levels of mesh refinement using quadrilateral and triangular cells. Top row: Regular meshes, Bottom row: Distorted meshes.

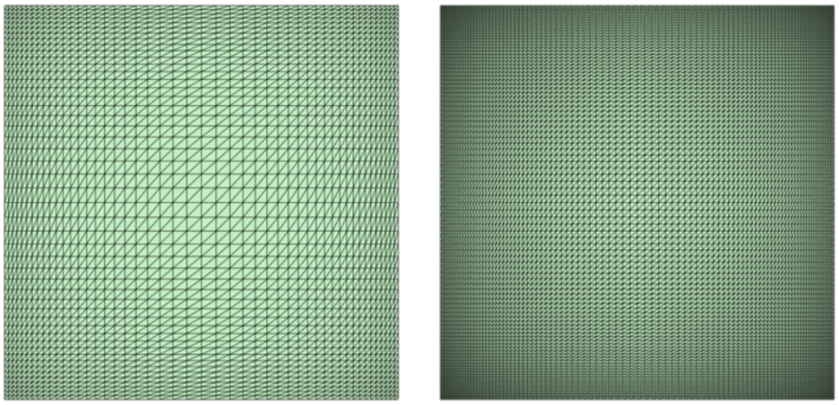

(a) (b)

FIGURE 12 | Cavity flow—(a) First and (b) second level of mesh refinement.

approximation and compare its performance with the FCFV approach [14]. More precisely, Lax-Friedrichs (LF) and Harten-Lax-van Leer (HLL) Riemann solvers, see (17), are employed. The nonlinear problem is solved using the Newton-Raphson algorithm, with a tolerance of 10^{-10}.

The outcome of the hybrid pressure formulation is compared to the FCFV method [14], a Taylor-Hood (Q2Q1) finite element result with streamline-upwind Petrov-Galerkin (SUPG) stabilization [34] and the reference solution by Ghia and co-workers [45]. On the one hand, the computational meshes (see Figure 12) for the hybrid pressure and FCFV formulations are characterized by a local refinement near the boundaries, with the height of the first layer of boundary cells being $10^{-2}/i$ for the i-th level of mesh refinement and the growth ratio ranging from 1.06 in the coarse mesh to 1.003 in the finest mesh. The resulting i-th mesh features $(24 \times 2^i) \times (24 \times 2^i) \times 2$ triangular cells. On the other hand, to compute the reference solution, a mesh of 700×700 quadrilateral cells is employed. This mesh sets the height of the first cell to 0.96×10^{-4} and features a local refinement near the four physical walls.

The quantities of interest in this problem are the profiles of velocity and pressure at the centerlines of the domain. Velocity profiles for $Re = 1,000$ are reported in Figure 13 for the third and fourth level of mesh refinement using LF and HLL stabilizations. For the sake of brevity, only meshes without distortion are presented. Using the LF Riemann solver, the results of the hybrid pressure and FCFV formulations are perfectly superposed, showing excellent agreement with the Taylor-Hood and Ghia et al. references (Figure 13a). As expected, the accuracy furtherly increases when the mesh is refined (Figure 13c). Alternatively, a more accurate

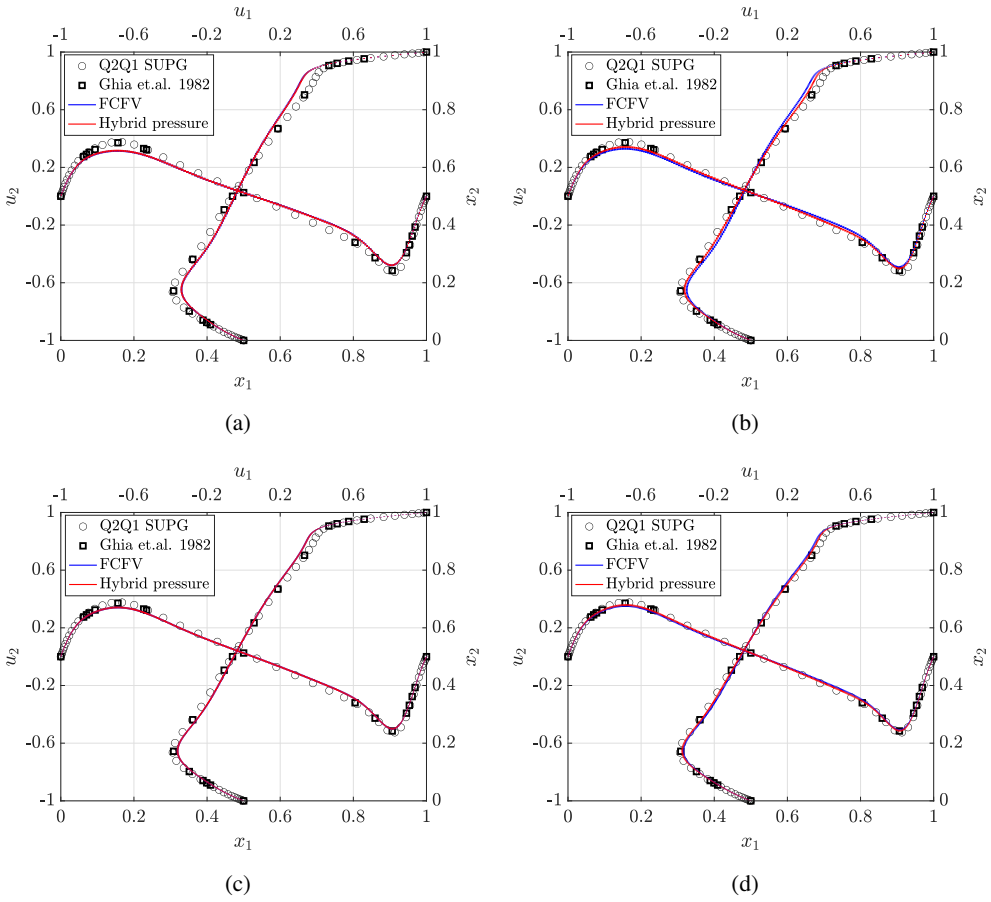

FIGURE 13 | Cavity flow at $Re = 1,000$ — Profiles of velocity along the centrelines using (a,c) Lax-Friedrichs and (b,d) Harten-Lax-van Leer Riemann solvers on different meshes. Top row: Third mesh, Bottom row: Fourth mesh.

approximation can be achieved on the coarse mesh by employing the HLL Riemann solver (Figure 13b), confirming the superior performance of this stabilization, already observed for the FCFV method [14]. In addition, it is worth noticing that the hybrid pressure formulation with HLL stabilization also provides slightly more accurate results with respect to the FCFV approximation with HLL on both meshes.

Nonetheless, it is in the approximation of p that the hybrid pressure formulation with HLL stabilization clearly shows its superior performance with respect to the FCFV scheme and the LF stabilization. Figure 14 displays the profiles of pressure at the centrelines for $Re = 1,000$. Whilst using LF Riemann solver the hybrid pressure formulation provides results comparable to the FCFV method and the fourth mesh is required to achieve an accurate description of pressure (Figure 14c), the HLL stabilization significantly improves the quality of the approximation, even on the coarser mesh (Figure 14b). Moreover, the hybrid pressure formulation clearly outperforms the FCFV method using the HLL Riemann solver: Using the third mesh, the hybrid pressure formulation with HLL stabilization provides results with accuracy comparable to the ones achieved by the FCFV scheme with HLL on the fourth level of mesh refinement, see Figure 14d, while reducing the number of cells from 294,912 to 73,728.

It is worth noticing that the quantities of interest reported in Figures 13 and 14 can be significantly influenced by local modifications of the flow field. To evaluate the global accuracy of the method, the errors of the hybrid pressure and FCFV formulations with respect to the Taylor-Hood solution are reported in Figure 15 as a function of the mesh size h. The results confirm that whilst the errors achieved by the two methods are comparable using the LF stabilization, the hybrid pressure clearly outperforms the FCFV scheme in the approximation of all variables when the HLL Riemann solver is employed.

Remark 8. The reference Taylor-Hood solution used to compute the errors of the FCFV and hybrid pressure formulation is obtained by simulating the so-called *leaky* cavity flow, given the strong imposition of the incompatible Dirichlet boundary conditions on the top left and top right corners. On the contrary, the FCFV and hybrid pressure formulations impose Dirichlet conditions at the barycentres of mesh faces, thus practically circumventing the incompatibility of these boundary conditions. It is worth noticing that the region affected by the incompatible Dirichlet boundary conditions in the Taylor-Hood solution features multiple cells and is reduced upon mesh refinement. This also affects the size of the region where pressure is non-zero, which shrinks tending to a pointwise singularity when $h \to 0$ [34]. To maintain a comparable reference Taylor-Hood solution for all meshes under analysis and to avoid introducing mesh-dependent artifacts in the error computation, the regions $[0, 0.05] \times [0.95, 1]$ and $[0.95, 1] \times [0.95, 1]$ are excluded from the domain Ω when computing the $\mathcal{L}_2(\Omega)$ norm of the error [14], as reported in Figure 15.

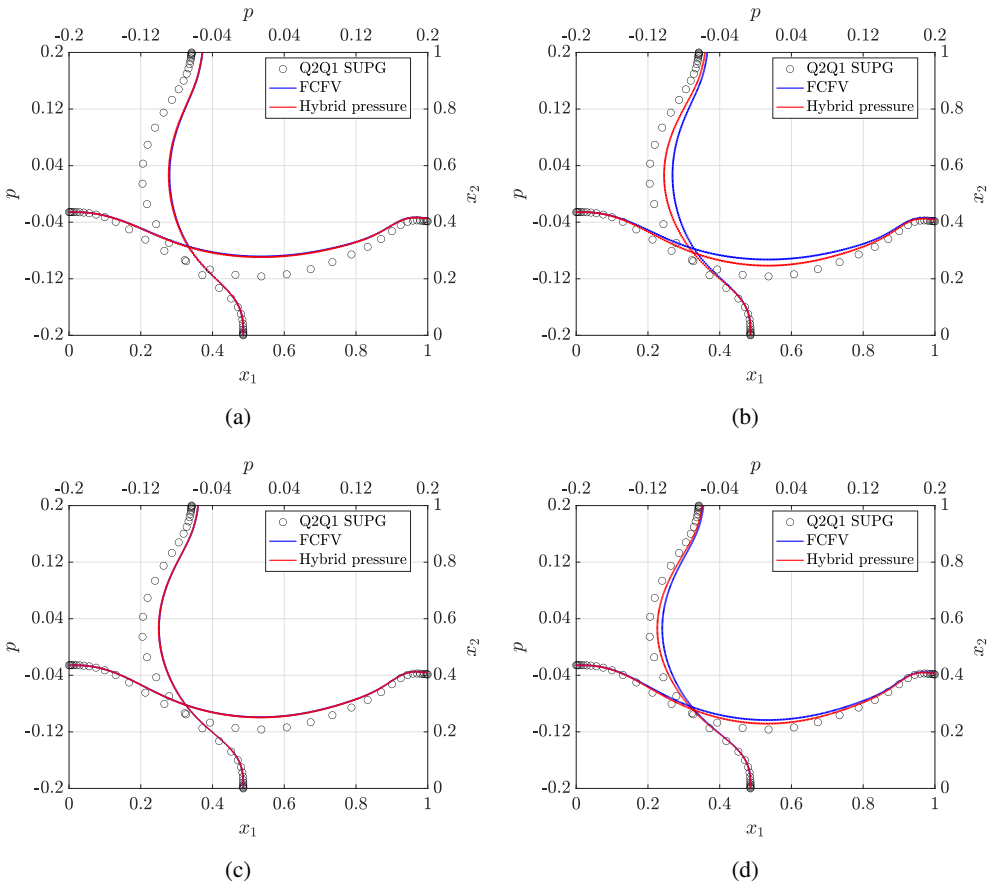

FIGURE 14 | Cavity flow at $Re = 1,000$ — Profiles of pressure along the centrelines using (a,c) Lax-Friedrichs and (b,d) Harten-Lax-van Leer Riemann solvers on different meshes. Top row: Third mesh, Bottom row: Fourth mesh.

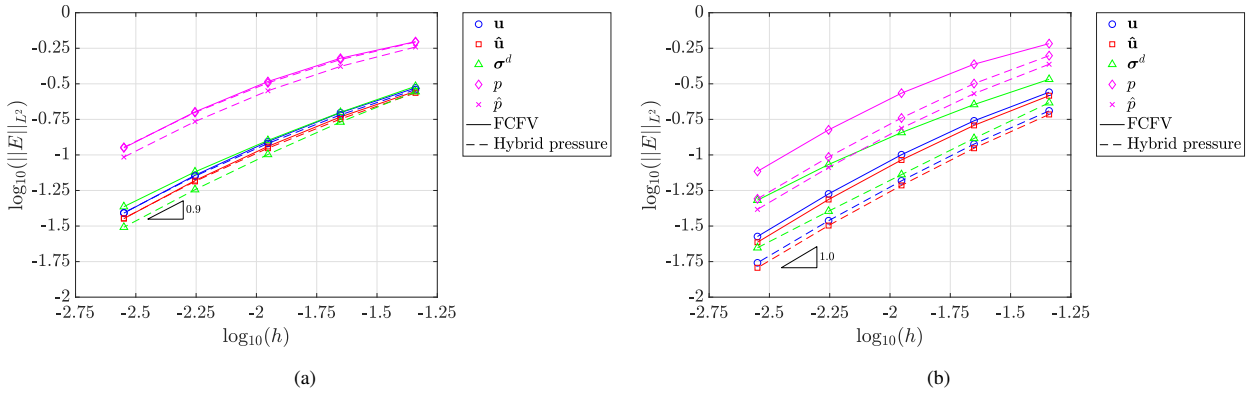

FIGURE 15 | Cavity flow at $Re = 1,000$ — Mesh convergence of the error of velocity, hybrid velocity, pressure, hybrid pressure, and deviatoric stress tensor, measured in the $\mathcal{L}_2$ norm as a function of the cell size h using (a) Lax-Friedrichs, (b) Harten-Lax-van Leer Riemann solvers.

Finally, Figure 16 presents the approximation of the cavity flow for Reynolds 3,200. Given the previously observed superiority of HLL with respect to LF, results are reported only for the HLL Riemann solver using the hybrid pressure formulation and the FCFV method. The profiles of velocity and pressure computed on the fourth mesh are displayed along the centrelines in Figure 16a,b, respectively. Also in this case, the hybrid pressure formulation outperforms the FCFV approach, achieving a slightly more accurate approximation of velocity while significantly improving the description of pressure.

The convergence of the relative $\mathcal{L}_2$ error, reported in Figure 16c for all the variables, confirms the superiority of the hybrid pressure formulation to construct an accurate face-based FV paradigm to simulate viscous laminar incompressible flows. Moreover, the accuracy appears to slightly increase at higher values of the Reynolds number, when convective effects are more relevant. Further studies, beyond the scope of the present work, need to be performed to evaluate the behavior of the proposed formulation in the turbulent regime. The closely related FCFV method was recently shown to be suitable for simulating

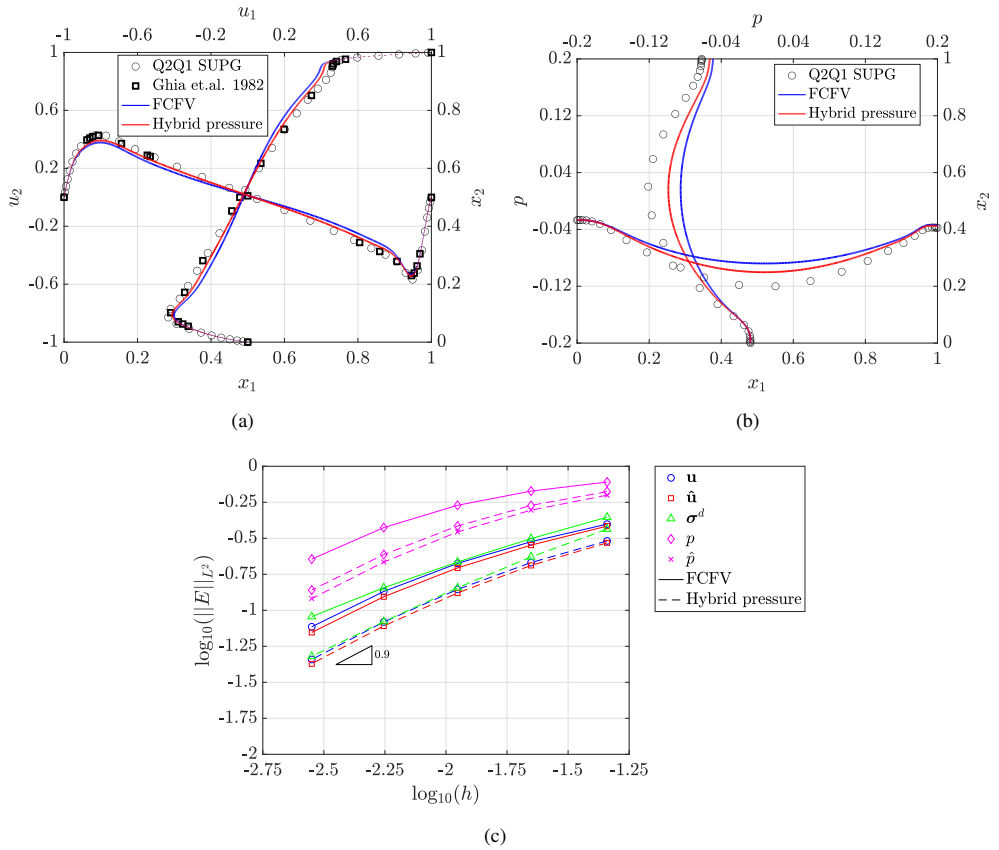

FIGURE 16 | Cavity flow at $Re = 3,200$—Approximation computed using Harten-Lax-van Leer Riemann solver. Profiles of (a) velocity and (b) pressure along the centrelines of the fourth mesh. (c) Mesh convergence of the error of velocity, hybrid velocity, pressure, hybrid pressure, and deviatoric stress tensor, measured in the $\mathcal{L}_2$ norm as a function of the cell size h.

turbulent incompressible flows using Reynolds-averaged Navier-Stokes equations with Spalart-Allmaras turbulence model [14].

6.4 | Three-Dimensional Navier-Stokes Flow Past a Sphere

The last example considers the steady-state incompressible Navier-Stokes flow past a three-dimensional sphere of diameter $D = 1$ at $Re = 20$. The computational domain is defined as $\Omega = ([-10D, 20D] \times [-10D, 10D] \times [-10D, 10D]) \setminus \mathcal{B}_{D/2,\mathbf{0}}$.

The case of $Re = 20$ is considered since this benchmark is well documented in the literature [46–48] and the symmetry of the flow with respect to the x_1x_2 and x_1x_3 planes is preserved for low values of the Reynolds number. Exploiting this symmetry, only one-fourth of the domain is simulated. A uniform horizontal velocity $\boldsymbol{u}_D = [1, 0, 0]^T$ is set on the inlet plane Γ_D at $x_1 = -10D$, a homogeneous Neumann condition is imposed on the outlet plane Γ_N at $x_1 = 20D$, whereas symmetry conditions are enforced on the remaining lateral surfaces Γ_S. The viscosity is selected as $\nu = 1/Re$, using D as characteristic length and the magnitude of $\boldsymbol{u}_D$ as characteristic velocity of the problem. It is worth recalling that the convective effects in the Navier-Stokes flow are responsible for breaking the symmetry of the velocity and pressure fields with respect to the x_2x_3 plane. In particular, to accurately capture the flow features, an appropriate local refinement of the mesh is required in the wake of the cylinder, as displayed in Figure 17a for the fourth mesh. In addition, Figure 17 reports the magnitude of the velocity, the streamlines, and the pressure field computed using the hybrid pressure formulation with HLL Riemann solver on the fourth level of mesh refinement described below.

To perform a mesh convergence study of the drag coefficient, five unstructured meshes of tetrahedral cells are constructed using `Gmsh` [49]. Table 4 reports the specifics of the mesh construction, including number of cells, $\mathtt{n}_{\mathtt{el}}$, number of faces, $\mathtt{n}_{\mathtt{fa}} = \mathtt{n}^{\mathcal{I}}_{\mathtt{fa}} + \mathtt{n}^{\mathcal{D}}_{\mathtt{fa}} + \mathtt{n}^{\mathcal{C}}_{\mathtt{fa}}$ (subdivided in the subset $\mathcal{I}$, $\mathcal{D}$, and $\mathcal{C}$), as well as the local cell size in the first layer near the wall, in the wake of the cylinder, and the farfield.

The dimensions of the resulting systems are detailed in Table 5. For the problem under analysis the number of unknowns for the hybrid velocity are given by $\mathtt{n}^{\hat{u}}_{\mathtt{dof}} = 3(\mathtt{n}^{\mathcal{I}}_{\mathtt{fa}} + \mathtt{n}^{\mathcal{C}}_{\mathtt{fa}})$, whereas the unknowns for hybrid pressure and pressure are $\mathtt{n}^{\hat{p}}_{\mathtt{dof}} = \mathtt{n}_{\mathtt{fa}}$, and $\mathtt{n}^{p}_{\mathtt{dof}} = \mathtt{n}_{\mathtt{el}}$, respectively. Hence, the number of degrees of freedom is $\mathtt{n}^{\hat{u}}_{\mathtt{dof}} + \mathtt{n}^{\hat{p}}_{\mathtt{dof}}$ for the hybrid pressure formulation and $\mathtt{n}^{\hat{u}}_{\mathtt{dof}} + \mathtt{n}^{p}_{\mathtt{dof}}$ for the FCFV method.

The convergence of the drag coefficient C_d is displayed in Figure 18 using the hybrid pressure formulation with HLL stabilization on the five meshes described above. The Newton-Raphson algorithm is employed to solve the nonlinear

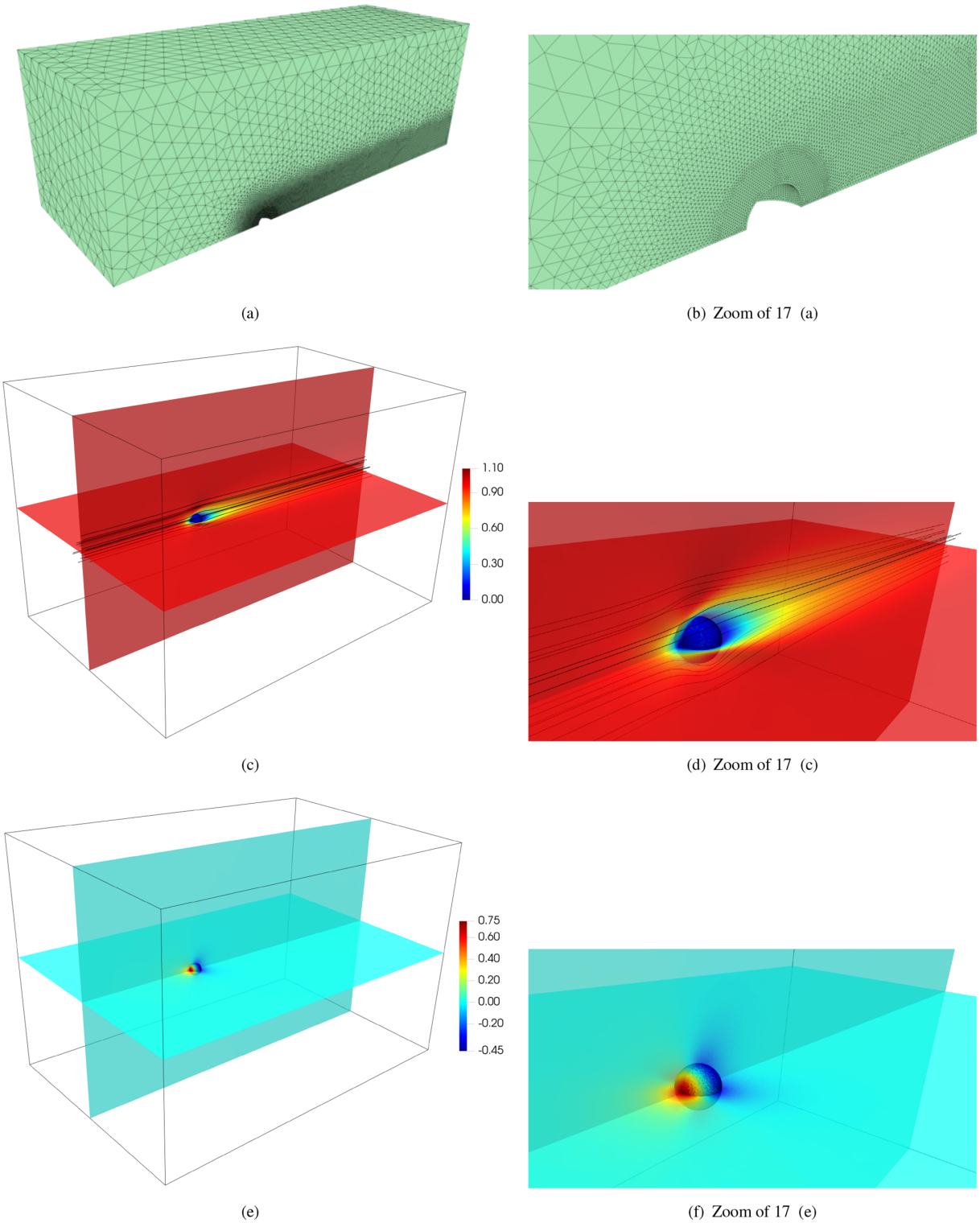

(a) (b) Zoom of 17 (a)

(c) (d) Zoom of 17 (c)

(e) (f) Zoom of 17 (e)

FIGURE 17 | Flow past a sphere at $Re = 20$—(a,b) Mesh; (c,d) Velocity magnitude and streamlines; (e,f) Pressure. (a), (b) Zoom of 17 (a), (c), (d) Zoom of 17 (c), (e), (f) Zoom of 17 (e).

problem, with a tolerance of 10^{-10}. The results show that, even on the coarsest mesh, the prediction provided by the hybrid pressure formulation lies within the range of values reported in the literature [46–48], whereas the FCFV method requires the fourth level of mesh refinement to achieve a precision in such an interval. In addition, although the values of the pressure part, C_{d_p}, and the viscous part, C_{d_v}, of the drag coefficient computed using the FCFV method on the first mesh are closer to the corresponding expected values, the hybrid pressure formulation outperforms the FCFV method by providing a faster and almost monotonic convergence of both components. Table 6 reports the detailed evolution of the drag coefficients and the reference values from the literature, showing excellent agreement of the hybrid pressure formulation.

TABLE 4 | Flow past a sphere at $Re = 20$—specifics of the computational meshes.

Mesh	n_{el}	Faces				First wall cell height	Wake cell size	Farfield cell size
		$n_{fa}^{\mathcal{I}}$	$n_{fa}^{\mathcal{D}}$	$n_{fa}^{\mathcal{C}}$	n_{fa}			
1	16,108	30,305	230	3,592	34,127	0.32	1.2	1.2
2	32,550	62,136	280	5,648	68,064	0.16	0.8	1.2
3	110,567	214,870	516	12,012	227,398	0.08	0.4	1.2
4	473,710	931,437	1,446	30,520	963,403	0.04	0.2	1.2
5	2,204,960	4,364,550	5,100	85,636	4,455,286	0.02	0.1	1.2

TABLE 5 | Flow past a sphere at $Re = 20$—comparison of the number of degrees of freedom of the hybrid pressure and FCFV formulations.

Mesh	$n_{dof}^{\hat{u}}$	Hybrid pressure		FCFV	
		$n_{dof}^{\hat{p}}$	n_{dof}	n_{dof}^{p}	n_{dof}
1	101,691	34,127	135,818	16,108	117,799
2	203,352	68,064	271,416	32,550	235,902
3	680,646	227,398	908,044	110,567	791,213
4	2,885,871	963,403	3,849,274	473,710	3,359,581
5	13,350,558	4,455,286	17,805,844	2,204,959	15,555,517

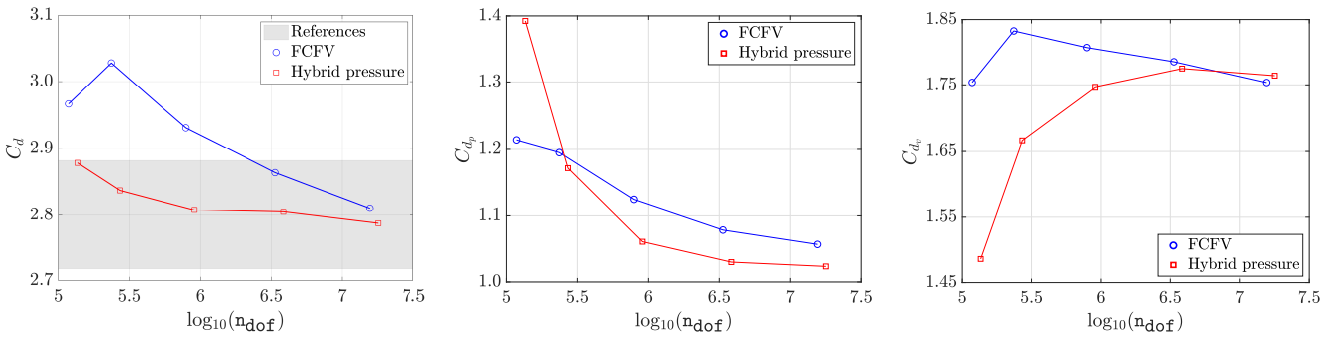

(a) (b) (c)

FIGURE 18 | Flow past a sphere at $Re = 20$—Convergence of (a) drag coefficient, (b) pressure part, and (c) viscous part of the drag coefficient as a function of the number of degrees of freedom in the simulation. The shaded area identifies the range of reference values published in the literature for this benchmark.

TABLE 6 | Flow past a sphere at $Re = 20$—mesh convergence of the drag coefficient C_d, its pressure part C_{d_p} and its viscous part C_{d_v}.

Mesh	C_d		C_{d_p}		C_{d_v}	
	Hybrid pressure	FCFV	Hybrid pressure	FCFV	Hybrid pressure	FCFV
1	2.878	2.967	1.392	1.213	1.486	1.754
2	2.837	3.028	1.171	1.195	1.666	1.833
3	2.808	2.931	1.061	1.124	1.747	1.807
4	2.805	2.864	1.030	1.078	1.775	1.785
5	2.788	2.810	1.023	1.057	1.764	1.754
	Literature					
[46]	2.790					
[47]	2.724					
[48]	[2.719, 2.882]					

TABLE 7 | Flow past a sphere at $Re = 20$—drag coefficient and estimated error for the total drag C_d, its pressure part C_{d_p} and its viscous part C_{d_v}.

	Hybrid pressure					
Mesh	C_d	ε_d	C_{d_p}	ε_{d_p}	C_{d_v}	ε_{d_v}
1	2.878	0.032	1.392	0.361	1.486	0.158
2	2.837	0.018	1.171	0.145	1.666	0.056
3	2.808	0.007	1.061	0.037	1.747	0.010
4	2.805	0.006	1.030	0.007	1.775	0.006
5	2.788	—	1.023	—	1.764	—
	FCFV					
Mesh	C_d	ε_d	C_{d_p}	ε_{d_p}	C_{d_v}	ε_{d_v}
1	2.967	0.056	1.213	0.148	1.754	0.000
2	3.028	0.078	1.195	0.131	1.833	0.045
3	2.931	0.043	1.124	0.063	1.807	0.030
4	2.864	0.019	1.078	0.020	1.785	0.018
5	2.810	—	1.057	—	1.754	—

To verify the mesh-convergence of the computations, the error on the total drag, as well as its pressure and viscous contribution, is estimated using the last mesh as the reference result. More precisely the estimated error on the i-th mesh is measured as

$$\varepsilon_{\diamond}^{i} := \frac{|C_{\diamond}^{i} - C_{\diamond}^{5}|}{|C_{\diamond}^{5}|} \tag{33}$$

Table 7 displays the estimated error for the first four meshes.

As qualitatively observed in Figure 18, the hybrid pressure formulation achieves convergence on the fourth mesh, assuming a desired error of 1% for both the pressure and viscous components of the drag. On the contrary, for the FCFV, the estimated error on the fourth mesh is still above the desired error, showing that further mesh refinement is required and confirming the superiority of the hybrid pressure formulation in approximating pressure in incompressible flows. It is worth noting that the same conclusions are obtained if the error is measured on the total drag. However, it is preferred to use a more restrictive criterion based on pressure and viscous components, because adding the pressure and viscous component of the drag can lead to error cancellation in the total drag.

Finally, a comparison of the computational cost of the hybrid pressure formulation relative to the FCFV method is provided. From Table 5, it is evident that, for a given mesh, the hybrid pressure formulation has more degrees of freedom than the FCFV approach.

For instance, consider the fourth level of mesh refinement—the coarsest mesh for which the FCFV method provides a C_d prediction within the range of values reported in the literature. For this mesh (Mesh 4), the global problem in the hybrid pressure formulation involves 17,805,844 unknowns, compared to 15,555,517 in the FCFV method. Consequently, for the same mesh, the hybrid pressure formulation is computationally more expensive than the FCFV approach.

Nonetheless, it is more reasonable to compare the methods based on a fixed level of accuracy. For a similar accuracy, the hybrid pressure formulation clearly outperforms the FCFV approach [14] in terms of computing cost. Specifically, Figure 18a shows that the hybrid pressure formulation can use Mesh 2 to achieve a C_d prediction comparable—if not slightly better—than that provided by the FCFV method on the fourth mesh. Using one computing node with 16 processors[1], building and assembling the global problem takes 2.1 s for the hybrid pressure formulation and 19.6 s for the FCFV method. Moreover, as highlighted in Section 5, the most computationally expensive task is solving the nonlinear global problem. The hybrid pressure and FCFV methods, respectively, require 3.1 s and 128.4 s to solve the global system in each Newton-Raphson iteration.

7 | Concluding Remarks

This work presented a new hybrid pressure face-centred finite volume solver for viscous laminar incompressible flows. The method relies on a mixed hybrid FV formulation in which the cell variables (velocity, pressure, and deviatoric strain rate tensor) are expressed in terms of the face velocity and the face pressure by means of a hybridization procedure. To do so, incompressibility is enforced weakly, and a new definition of the inter-cell mass flux is proposed. The resulting method has been tested on a suite of 2D and 3D benchmark problems for the steady-state incompressible Navier-Stokes equations.

First, a linear problem (i.e., Stokes equations) with a synthetic solution was used to verify the first-order convergence of velocity, pressure, and deviatoric stress tensor on meshes of quadrilateral and triangular cells. The effect of cell distortion and the sensitivity of the method to the choice of the stabilization coefficient were also assessed.

Whilst for Stokes flows the hybrid pressure formulation provides results comparable to the FCFV method, its performance is clearly superior in the presence of convection phenomena.

Upon verifying, by means of a synthetic problem, that optimal convergence of the discrete solution was also achieved in the Navier-Stokes setting, the cavity flow was studied for Reynolds numbers up to 3,200. These tests showcased the superiority of the hybrid pressure formulation with respect to traditional FCFV schemes when convective effects are relevant. The hybrid pressure approach with HLL Riemann solver is indeed capable of providing accurate predictions on meshes coarser than the ones required by the FCFV method. Finally, the flow past a sphere at $Re = 20$ was used to confirm the superior performance of the hybrid pressure approach with respect to the FCFV scheme, also in 3D. Numerical results showed the suitability of the method to compute quantities of engineering interest (i.e., the drag coefficient), using unstructured tetrahedral meshes and achieving sufficient accuracy, in excellent agreement with the reference values published in the literature.

Some computational aspects of the method have also been discussed, numerically studying the properties of the spectrum of the matrix for different cell types, for uniform and distorted meshes. The experimental observations yielded the conjecture that the matrix obtained from the global problem of the hybrid pressure formulation is negative definite. Future work will focus on a more thorough analysis of these properties, with the goal of developing efficient iterative schemes and preconditioners tailored to the presented hybrid pressure FCFV formulation.

Acknowledgments

The authors acknowledge the support of: Generalitat de Catalunya that partially funded the PhD scholarship of DC; H2020 MSCA ITN-EJD ProTechTion (Grant No. 764636) that partially funded the PhD scholarship of L.M.V.; Spanish Ministry of Science, Innovation and Universities and Spanish State Research Agency MICIU/AEI/10.13039/501100011033 (Grants No. PID2020-113463RB-C33 to M.G., PID2020-113463RB-C32 to A.H. and CEX2018-000797-S to M.G. and A.H.); Generalitat de Catalunya (Grant No. 2021-SGR-01049 to M.G. and A.H.); M.G. is Fellow of the Serra Húnter Programme of the Generalitat de Catalunya.

Data Availability Statement

The authors have nothing to report.

Endnotes

[1] 2 × 8-Core Xeon Gold 6134 (3.20 GHz/25MB cache, 2666MHz FSB) with 192 GB RAM.

References

1. Z. Wang, K. Fidkowski, R. Abgrall, et al., "High-Order CFD Methods: Current Status and Perspective," *International Journal for Numerical Methods in Fluids* 72, no. 8 (2013): 811–845.

2. R. Abgrall and M. Ricchiuto, "High Order Methods for CFD," in *Encyclopedia of Computational Mechanics Second Edition*, ed. E. Stein, R. de Borst, and T. Hughes (John Wiley & Sons, Limited, 2017), 1–54.

3. K. Fidkowski, P. O. Persson, and N. Nguyen, "Special Issue: Advances in High-Order Methods for CFD," *International Journal of Computational Fluid Dynamics* 37, no. 6 (2023): 429.

4. R. Leveque, *Finite Volume Methods for Hyperbolic Problems* (Cambridge University Press, 2013).

5. T. Barth, R. Herbin, and M. Ohlberger, "Finite Volume Methods: Foundation and Analysis," in *Encyclopedia of Computational Mechanics Second Edition*, ed. E. Stein, R. de Borst, and T. Hughes (John Wiley & Sons, Limited, 2017), 1–60.

6. B. Diskin, J. Thomas, E. Nielsen, H. Nishikawa, and J. White, "Comparison of Node-Centered and Cell-Centered Unstructured Finite-Volume Discretizations: Viscous Fluxes," *AIAA Journal* 48, no. 7 (2010): 1326.

7. B. Diskin and J. Thomas, "Comparison of Node-Centered and Cell-Centered Unstructured Finite-Volume Discretizations: Inviscid Fluxes," *AIAA Journal* 49, no. 4 (2011): 836–854.

8. R. Sevilla, M. Giacomini, and A. Huerta, "A Face-Centred Finite Volume Method for Second-Order Elliptic Problems," *International Journal for Numerical Methods in Engineering* 115, no. 8 (2018): 986–1014.

9. R. Sevilla, M. Giacomini, and A. Huerta, "A Locking-Free Face-Centred Finite Volume (FCFV) Method for Linear Elastostatics," *Computers & Structures* 212 (2019): 43–57.

10. R. Sevilla and T. Duretz, "A Face-Centred Finite Volume Method for High-Contrast Stokes Interface Problems," *International Journal for Numerical Methods in Engineering* 124, no. 17 (2023): 3709–3732.

11. R. Sevilla and T. Duretz, "Face-Centred Finite Volume Methods for Stokes Flows With Variable Viscosity," *International Journal for Numerical Methods in Engineering* 125, no. 10 (2024): e7450.

12. J. Vila-Pérez, M. Giacomini, R. Sevilla, and A. Huerta, "A Non-Oscillatory Face-Centred Finite Volume Method for Compressible Flows," *Computers & Fluids* 235 (2022): 105272, https://doi.org/10.1016/j.compfluid.2021.105272.

13. J. Vila-Pérez, M. Giacomini, and A. Huerta, "Benchmarking the Face-Centred Finite Volume Method for Compressible Laminar Flows," *International Journal of Numerical Methods for Heat & Fluid Flow* 33, no. 6 (2023): 2198–2231.

14. L. Vieira, M. Giacomini, R. Sevilla, and A. Huerta, "A Face-Centred Finite Volume Method for Laminar and Turbulent Incompressible Flows," *Computers & Fluids* 279 (2024): 106339.

15. D. Cortellessa, M. Giacomini, and A. Huerta, "An OpenFOAM Face-Centred Solver for Incompressible Flows Robust to Mesh Distortion," in *Emerging Technologies in Computational Sciences for Industry, Sustainability and Innovation*, ed. M. Giacomini, S. Perotto, and G. Rozza (Springer Cham, 2025).

16. L. Vieira, M. Giacomini, R. Sevilla, and A. Huerta, "A Second-Order Face-Centred Finite Volume Method for Elliptic Problems," *Computer Methods in Applied Mechanics and Engineering* 358 (2020): 112655.

17. M. Giacomini and R. Sevilla, "A Second-Order Face-Centred Finite Volume Method on General Meshes With Automatic Mesh Adaptation," *International Journal for Numerical Methods in Engineering* 121, no. 23 (2020): 5227–5255.

18. B. Cockburn and J. Gopalakrishnan, "A Characterization of Hybridized Mixed Methods for Second Order Elliptic Problems," *SIAM Journal on Numerical Analysis* 42, no. 1 (2004): 283–301.

19. B. Cockburn, J. Gopalakrishnan, and R. Lazarov, "Unified Hybridization of Discontinuous Galerkin, Mixed, and Continuous Galerkin Methods for Second Order Elliptic Problems," *SIAM Journal on Numerical Analysis* 47, no. 2 (2009): 1319–1365.

20. B. Cockburn, "Static Condensation, Hybridization, and the Devising of the HDG Methods," in *Building Bridges: Connections and Challenges in Modern Approaches to Numerical Partial Differential Equations*, vol. 114, ed. G. Barrenechea, F. Brezzi, A. Cangiani, and E. Georgoulis (Springer, 2016), 129–177.

21. M. Giacomini, R. Sevilla, and A. Huerta, "HDGlab: An Open-Source Implementation of the Hybridisable Discontinuous Galerkin Method in MATLAB," *Archives of Computational Methods in Engineering* 28, no. 3 (2021): 1941–1986.

22. N. Nguyen, J. Peraire, and B. Cockburn, "A Hybridizable Discontinuous Galerkin Method for Stokes Flow," *Computer Methods in Applied Mechanics and Engineering* 199, no. 9–12 (2010): 582–597.

23. N. Nguyen, J. Peraire, and B. Cockburn, "An Implicit High-Order Hybridizable Discontinuous Galerkin Method for the Incompressible Navier-Stokes Equations," *Journal of Computational Physics* 230, no. 4 (2011): 1147–1170.

24. G. Giorgiani, S. Fernández-Méndez, and A. Huerta, "Hybridizable Discontinuous Galerkin With Degree Adaptivity for the Incompressible Navier–Stokes Equations," *Computers & Fluids* 98 (2014): 196–208.

25. M. Giacomini, A. Karkoulias, R. Sevilla, and A. Huerta, "A Superconvergent HDG Method for Stokes Flow With Strongly Enforced Symmetry of the Stress Tensor," *Journal of Scientific Computing* 77, no. 3 (2018): 1679–1702.

26. B. Cockburn and J. Gopalakrishnan, "The Derivation of Hybridizable Discontinuous Galerkin Methods for Stokes Flow," *SIAM Journal on Numerical Analysis* 47, no. 2 (2009): 1092–1125.

27. A. La Spina, M. Kronbichler, M. Giacomini, W. Wall, and A. Huerta, "A Weakly Compressible Hybridizable Discontinuous Galerkin Formulation for Fluid-Structure Interaction Problems," *Computer Methods in Applied Mechanics and Engineering* 372 (2020): 113392.

28. J. Vila-Pérez, M. Giacomini, R. Sevilla, and A. Huerta, "Hybridisable Discontinuous Galerkin Formulation of Compressible Flows," *Archives of Computational Methods in Engineering* 28, no. 2 (2021): 753–784.

29. A. La Spina and J. Fish, "A Superconvergent Hybridizable Discontinuous Galerkin Method for Weakly Compressible Magnetohydrodynamics," *Computer Methods in Applied Mechanics and Engineering* 388 (2022): 114278.

30. M. Giacomini, R. Sevilla, and A. Huerta, "Tutorial on Hybridizable Discontinuous Galerkin (HDG) Formulation for Incompressible Flow Problems," in *Modeling in Engineering Using Innovative Numerical Methods for Solids and Fluids*, vol. 599, ed. L. De Lorenzis and A. Düster (Springer International Publishing, 2020), 163–201.

31. S. Rhebergen and B. Cockburn, "A Space–Time Hybridizable Discontinuous Galerkin Method for Incompressible Flows on Deforming Domains," *Journal of Computational Physics* 231, no. 11 (2012): 4185–4204.

32. R. Labeur and G. Wells, "Energy Stable and Momentum Conserving Hybrid Finite Element Method for the Incompressible Navier–Stokes Equations," *SIAM Journal on Scientific Computing* 34, no. 2 (2012): A889–A913.

33. S. Rhebergen and G. Wells, "A Hybridizable Discontinuous Galerkin Method for the Navier–Stokes Equations With Pointwise Divergence-Free Velocity Field," *Journal of Scientific Computing* 76, no. 3 (2018): 1484–1501.

34. J. Donea and A. Huerta, *Finite Element Methods for Flow Problems* (John Wiley & Sons, Limted, 2003).

35. R. Sevilla, M. Giacomini, A. Karkoulias, and A. Huerta, "A Superconvergent Hybridisable Discontinuous Galerkin Method for Linear Elasticity," *International Journal for Numerical Methods in Engineering* 116, no. 2 (2018): 91–116.

36. B. Cockburn and J. Gopalakrishnan, "Incompressible Finite Elements via Hybridization. I. The Stokes System in Two Space Dimensions," *SIAM Journal on Numerical Analysis* 43, no. 4 (2005): 1627–1650.

37. B. Cockburn, N. Nguyen, and J. Peraire, "A Comparison of HDG Methods for Stokes Flow," *Journal of Scientific Computing* 45, no. 1–3 (2010): 215–237.

38. A. Montlaur, S. Fernández-Méndez, and A. Huerta, "Discontinuous Galerkin Methods for the Stokes Equations Using Divergence-Free Approximations," *International Journal for Numerical Methods in Fluids* 57, no. 9 (2008): 1071–1092.

39. B. Cockburn, B. Dong, and J. Guzmán, "A Superconvergent LDG-Hybridizable Galerkin Method for Second-Order Elliptic Problems," *Mathematics of Computation* 77, no. 264 (2008): 1887–1916.

40. E. Toro, *Riemann Solvers and Numerical Methods for Fluid Dynamics* (Springer-Verlag, 2009).

41. R. Guyan, "Reduction of Stiffness and Mass Matrices," *AIAA Journal* 3, no. 2 (1965): 380.

42. B. Fraeijs de Veubeke, "Displacement and Equilibrium Models in the Finite Element Method," in *Stress Analysis*, ed. O. C. Zienkiewicz and G. S. Holister (John Wiley & Sons, 1965), 145–197.

43. S. Balay, S. Abhyankar, and M. F. Adams, *PETSc/TAO Users Manual*. Technical Report ANL-21/39–Revision 3.22 (Argonne National Laboratory, 2024).

44. S. Cheung, E. Chung, H. Kim, and Y. Qian, "Staggered Discontinuous Galerkin Methods for the Incompressible Navier–Stokes Equations," *Journal of Computational Physics* 302 (2015): 251–266.

45. U. Ghia, K. Ghia, and C. Shin, "High-Re Solutions for Incompressible Flow Using the Navier-Stokes Equations and a Multigrid Method," *Journal of Computational Physics* 48, no. 3 (1982): 387–411.

46. H. Schlichting and K. Gersten, *Boundary-Layer Theory* (Springer, 2016).

47. M. Tabata and K. Itakura, "A Precise Computation of Drag Coefficients of a Sphere," *International Journal of Computational Fluid Dynamics* 9, no. 3–4 (1998): 303–311.

48. A. Crivellini, V. D'Alessandro, and F. Bassi, "Assessment of a High-Order Discontinuous Galerkin Method for Incompressible Three-Dimensional Navier–Stokes Equations: Benchmark Results for the Flow Past a Sphere up to re= 500," *Computers & Fluids* 86 (2013): 442–458.

49. C. Geuzaine and J. F. Remacle, "Gmsh: A 3-D Finite Element Mesh Generator With Built-in Pre-and Post-Processing Facilities," *International Journal for Numerical Methods in Engineering* 79, no. 11 (2009): 1309–1331.

50. J. Fish and T. Belytschko, *A First Course in Finite Elements* (John Wiley and Sons Limited, 2007).

Appendix A

Implementation of the Pointwise Symmetry of the Mixed Variable

The symmetry of the mixed variable and the deviatoric stress tensor is imposed pointwise using Voigt notation [30, 50]. More precisely, to treat the $n_{sd} \times n_{sd}$ matrix representing $\mathbf{L}$, only $m_{sd} := n_{sd}(n_{sd}+1)/2$ non-redundant components are stored in the vector

$$\mathbf{L}_{\mathrm{V}} := \begin{cases} \left[L_{11},\ L_{22},\ L_{12}\right]^T & \text{in 2D,} \\ \left[L_{11},\ L_{22},\ L_{33},\ L_{12},\ L_{13},\ L_{23}\right]^T & \text{in 3D} \end{cases} \tag{A1}$$

Similarly, to represent the normal direction to a surface, the matrix $\mathbf{N}_{\mathrm{V}}$ is defined as

$$\mathbf{N}_{\mathrm{V}} := \begin{cases} \begin{bmatrix} n_1 & 0 & n_2 \\ 0 & n_2 & n_1 \end{bmatrix}^T & \text{in 2D,} \\ \begin{bmatrix} n_1 & 0 & 0 & n_2 & n_3 & 0 \\ 0 & n_2 & 0 & n_1 & 0 & n_3 \\ 0 & 0 & n_3 & 0 & n_1 & n_2 \end{bmatrix}^T & \text{in 3D} \end{cases} \tag{A2}$$

with n_k being the k-th component of the discrete outward unit normal vector $\mathbf{n}$.

It follows that the second-order tensor $\hat{\mathbf{u}}\mathbf{n}^T + \mathbf{n}\hat{\mathbf{u}}^T - \frac{2}{3}(\mathbf{n}^T\hat{\mathbf{u}})\mathbf{I}_{n_{sd}}$ associated with the computation of the mixed variable can be rewritten at the

discrete level using Voigt notation as $\mathbf{D}_{\mathrm{V}}\mathbf{N}_{\mathrm{V}}\hat{\mathbf{u}}$, where the matrix $\mathbf{D}_{\mathrm{V}}$ is given by

$$\mathbf{D}_{\mathrm{V}} := \begin{bmatrix} 2\mathbf{I}_{\mathtt{n}_{\mathtt{sd}}} - \frac{2}{3}\mathbf{J}_{\mathtt{n}_{\mathtt{sd}}} & \mathbf{0}_{\mathtt{n}_{\mathtt{sd}}\times\mathtt{n}_{\mathtt{rr}}} \\ \mathbf{0}_{\mathtt{n}_{\mathtt{rr}}\times\mathtt{n}_{\mathtt{sd}}} & \mathbf{I}_{\mathtt{n}_{\mathtt{rr}}} \end{bmatrix} \tag{A3}$$

$\mathbf{I}_m$ is the $m \times m$ identity matrix, $\mathbf{J}_\ell$ the $\ell \times \ell$ matrix with all components equal to 1, and $\mathtt{n}_{\mathtt{rr}} := \mathtt{n}_{\mathtt{sd}}(\mathtt{n}_{\mathtt{sd}}-1)/2$ denotes the number of rigid body rotations as a function of the number of spatial dimensions $\mathtt{n}_{\mathtt{sd}}$.

Hence, the vectorized form of the first equation in Equation (22a) yields the residual

$$\mathbf{R}_{e,L} = |\Omega_e|\mathbf{L}_{\mathrm{V},e} + \sum_{j\in D_e} |\Gamma_{e,j}|\mathbf{D}_{\mathrm{V}}\mathbf{N}_{\mathrm{V},j}\mathbf{u}_{D,j} + \sum_{j\in B_e} |\Gamma_{e,j}|\mathbf{D}_{\mathrm{V}}\mathbf{N}_{\mathrm{V},j}\hat{\mathbf{u}}_j \tag{A4a}$$

for the computation of the mixed variable, whereas the residual of the global problem associated with the inter-cell continuity of the momentum flux (see first equation in Equation (22b)) is given by

$$\begin{aligned} \mathbf{R}_{e,i,\hat{u}} = |\Gamma_{e,i}|\Big\{ \Big(\nu\mathbf{N}_{\mathrm{V},i}^T\mathbf{L}_{\mathrm{V},e} + \boldsymbol{\tau}_i\mathbf{u}_e - \boldsymbol{\tau}_i\hat{\mathbf{u}}_i\Big)\chi_{I_e}(i) + \hat{\mathbf{B}}_i\chi_{C_e}(i)\Big\} \\ d \quad \text{for all } i \in \mathcal{B}_e \end{aligned} \tag{A4b}$$

The remaining residuals $\mathbf{R}_{e,u}$, $\mathbf{R}_{e,p}$, and $\mathbf{R}_{e,i,\hat{p}}$ maintain the definitions in Equation (22). Finally, the discrete boundary operator (23) is rewritten using Voigt notation as

$$\hat{\mathbf{B}}_i = \begin{cases} \hat{\mathrm{p}}_i\mathbf{n}_i + \nu\mathbf{N}_{\mathrm{V},i}^T\mathbf{L}_{\mathrm{V},e} + \boldsymbol{\tau}_i^d(\mathbf{u}_e - \hat{\mathbf{u}}_i) + \mathbf{g}_i & \text{for } i \in \mathcal{N}_e, \\ \left\{ \begin{matrix} \mathbf{t}_{k,i}^T[\nu\mathbf{N}_{\mathrm{V},i}^T\mathbf{L}_{\mathrm{V},e} + \boldsymbol{\tau}_i^d(\mathbf{u}_e - \hat{\mathbf{u}}_i)] \\ \mathbf{n}_i^T\hat{\mathbf{u}}_i \end{matrix} \right\} & \text{for } i \in \mathcal{S}_e, \\ & \text{and for } k = 1, \ldots, \mathtt{n}_{\mathtt{sd}} - 1 \end{cases} \tag{A5}$$

Appendix B

Hybrid Pressure FCFV Method for the Stokes Equations

For highly viscous flows, the convection term in Equation (1) is negligible and the resulting Stokes equations can be written as

$$\begin{cases} -\boldsymbol{\nabla}\cdot\boldsymbol{\sigma} &= \boldsymbol{s} \quad \text{in } \Omega, \\ \boldsymbol{\nabla}\cdot\boldsymbol{u} &= 0 \quad \text{in } \Omega, \\ \boldsymbol{B}(\boldsymbol{\varepsilon}^d, \boldsymbol{u}, p) &= \mathbf{0} \quad \text{on } \partial\Omega \end{cases} \tag{B1}$$

with $\nu = 1$, while maintaining the definitions of the Cauchy stress tensor and the boundary conditions introduced in Section 2.

In this case, the local and global problems (19a) and (19b) respectively reduce to

$$\begin{cases} -\int_{\Omega_e} \boldsymbol{L}\, d\Omega &= \int_{\partial\Omega_e\cap\Gamma_D} \Big(\boldsymbol{u}_D\otimes\boldsymbol{n} + \boldsymbol{n}\otimes\boldsymbol{u}_D - \frac{2}{3}(\boldsymbol{u}_D\cdot\boldsymbol{n})\mathbf{I}_{\mathtt{n}_{\mathtt{sd}}}\Big)d\Gamma \\ &\quad + \int_{\partial\Omega_e\setminus\Gamma_D} \Big(\hat{\boldsymbol{u}}\otimes\boldsymbol{n} + \boldsymbol{n}\otimes\hat{\boldsymbol{u}} - \frac{2}{3}(\hat{\boldsymbol{u}}\cdot\boldsymbol{n})\mathbf{I}_{\mathtt{n}_{\mathtt{sd}}}\Big)d\Gamma, \\ \int_{\partial\Omega_e} \boldsymbol{\tau}^d\boldsymbol{u}\, d\Gamma &= \int_{\Omega_e} \boldsymbol{s}\, d\Omega + \int_{\partial\Omega_e\cap\Gamma_D} \boldsymbol{\tau}^d\boldsymbol{u}_D\, d\Gamma \\ &\quad + \int_{\partial\Omega_e\setminus\Gamma_D} \boldsymbol{\tau}^d\,\hat{\boldsymbol{u}}\, d\Gamma - \int_{\partial\Omega_e} \hat{\boldsymbol{p}}\boldsymbol{n}\, d\Gamma, \\ -\int_{\partial\Omega_e} \tau^p p\, d\Gamma &= \int_{\partial\Omega_e\cap\Gamma_D} \boldsymbol{u}_D\cdot\boldsymbol{n}\, d\Gamma + \int_{\partial\Omega_e\setminus\Gamma_D} \hat{\boldsymbol{u}}\cdot\boldsymbol{n}\, d\Gamma - \int_{\partial\Omega_e} \tau^p\hat{p}\, d\Gamma \end{cases} \tag{B2a}$$

and

$$\begin{cases} \sum_{e=1}^{\mathtt{n}_{\mathtt{el}}} \Big\{ \int_{\partial\Omega_e\setminus\partial\Omega} \nu\boldsymbol{L}\boldsymbol{n}\, d\Gamma + \int_{\partial\Omega_e\setminus\partial\Omega} \boldsymbol{\tau}^d\boldsymbol{u}\, d\Gamma \\ \quad - \int_{\partial\Omega_e\setminus\partial\Omega} \boldsymbol{\tau}^d\,\hat{\boldsymbol{u}}\, d\Gamma + \int_{\partial\Omega_e\cap\partial\Omega\setminus\Gamma_D} \hat{\boldsymbol{B}}(\boldsymbol{L},\boldsymbol{u},\hat{\boldsymbol{u}},\hat{p})\, d\Gamma \Big\} = \mathbf{0}, \\ \sum_{e=1}^{\mathtt{n}_{\mathtt{el}}} \Big\{ \int_{\partial\Omega_e} \tau^p p\, d\Gamma - \int_{\partial\Omega_e} \tau^p\hat{p}\, d\Gamma \Big\} = 0 \end{cases} \tag{B2b}$$

where the trace of the boundary operator is defined in Equation (18).

The discretization of Equation (B.7) following the strategy in Section 4 and exploiting Voigt notation for the mixed variable as described in Appendix A yields the linear local problem

$$\begin{cases} -|\Omega_e|\mathbf{L}_{\mathrm{V},e} &= \sum_{j\in D_e} |\Gamma_{e,j}|\mathbf{D}_{\mathrm{V}}\mathbf{N}_{\mathrm{V},j}\mathbf{u}_{D,j} + \sum_{j\in B_e} |\Gamma_{e,j}|\mathbf{D}_{\mathrm{V}}\mathbf{N}_{\mathrm{V},j}\hat{\mathbf{u}}_j, \\ \sum_{j\in\mathcal{A}_e} |\Gamma_{e,j}|\boldsymbol{\tau}_j^d\mathbf{u}_e &= |\Omega_e|\mathbf{s}_e + \sum_{j\in D_e} |\Gamma_{e,j}|\boldsymbol{\tau}_j^d\mathbf{u}_{D,j} \\ &\quad + \sum_{j\in B_e} |\Gamma_{e,j}|\boldsymbol{\tau}_j^d\,\hat{\mathbf{u}}_j - \sum_{j\in\mathcal{A}_e} |\Gamma_{e,j}|\hat{\mathrm{p}}_j\mathbf{n}_j, \\ -\sum_{j\in\mathcal{A}_e} |\Gamma_{e,j}|\tau_j^p\mathrm{p}_e &= \sum_{j\in D_e} |\Gamma_{e,j}|\mathbf{n}_j^T\mathbf{u}_{D,j} \\ &\quad + \sum_{j\in B_e} |\Gamma_{e,j}|\mathbf{n}_j^T\hat{\mathbf{u}}_j - \sum_{j\in\mathcal{A}_e} |\Gamma_{e,j}|\tau_j^p\hat{\mathrm{p}}_j \end{cases} \tag{B3a}$$

for $e = 1, \ldots, \mathtt{n}_{\mathtt{el}}$ and the linear global problem

$$\begin{cases} \sum_{e=1}^{\mathtt{n}_{\mathtt{el}}} |\Gamma_{e,i}|\Big\{ \Big(\nu\mathbf{N}_{\mathrm{V},i}^T\mathbf{L}_{\mathrm{V},e} + \boldsymbol{\tau}_i^d\mathbf{u}_e - \boldsymbol{\tau}_i^d\,\hat{\mathbf{u}}_i\Big) \\ \qquad \chi_{I_e}(i) + \hat{\mathbf{B}}_i\chi_{C_e}(i)\Big\} = \mathbf{0}, \ \text{for all } i \in \mathcal{B}_e, \\ \sum_{e=1}^{\mathtt{n}_{\mathtt{el}}} |\Gamma_{e,i}|\tau_i^p(\mathrm{p}_e - \hat{\mathrm{p}}_i) = 0, \ \text{for all } i \in \mathcal{A}_e \end{cases} \tag{B3b}$$

with the discrete boundary operator $\hat{\mathbf{B}}_i$ introduced in Equation (A5).

For the sake of readability, let us introduce the following quantities, exclusively depending on geometric information and user-defined data:

$$\mathbf{A}_u^e := \sum_{j\in\mathcal{A}_e} |\Gamma_{e,j}|\boldsymbol{\tau}_j^d, \qquad \mathrm{a}_p^e := \sum_{j\in\mathcal{A}_e} |\Gamma_{e,j}|\tau_j^p \tag{B4a}$$

$$\begin{aligned} \mathbf{f}^e{}_L &:= \sum_{j\in D_e} |\Gamma_{e,j}|\mathbf{D}_{\mathrm{V}}\mathbf{N}_{\mathrm{V},j}\mathbf{u}_{D,j}, \\ \mathbf{f}^e{}_u &:= |\Omega_e|\mathbf{s}_e + \sum_{j\in D_e} |\Gamma_{e,j}|\boldsymbol{\tau}_j^d\mathbf{u}_{D,j}, \\ \mathrm{f}^e{}_p &:= \sum_{j\in D_e} |\Gamma_{e,j}|\mathbf{n}_j^T\mathbf{u}_{D,j} \end{aligned} \tag{B4b}$$

Replacing the expressions of the cell unknowns $\mathbf{L}_{\mathrm{V}}$, $\mathbf{u}$, and $\mathbf{p}$ from Equation (B3a) into (B3b), it follows the linear system

$$\begin{bmatrix} \mathbf{K}_{\hat{u}\hat{u}} & \mathbf{K}_{\hat{u}\hat{p}} \\ \mathbf{K}_{\hat{p}\hat{u}} & \mathbf{K}_{\hat{p}\hat{p}} \end{bmatrix} \begin{Bmatrix} \hat{\mathbf{u}} \\ \hat{\mathbf{p}} \end{Bmatrix} = \begin{Bmatrix} \mathbf{f}_{\hat{u}} \\ \mathbf{f}_{\hat{p}} \end{Bmatrix} \tag{B5}$$

In order to compare the structure of system (B5) to equation 38 and 39 of the FCFV formulation [8], assume $\Gamma_S = \emptyset$. Hence, the blocks composing the matrix and the right-hand side are obtained by assembling the cell contributions

$$\begin{aligned} [\mathbf{K}_{\hat{u}\hat{u}}]_{i,j}^e &:= |\Gamma_{e,i}||\Gamma_{e,j}|\Big(-\nu|\Omega_e|^{-1}\mathbf{N}_{\mathrm{V},i}^T\mathbf{D}_{\mathrm{V}}\mathbf{N}_{\mathrm{V},j} + \boldsymbol{\tau}_i^d[\mathbf{A}_u^e]^{-1}\,\boldsymbol{\tau}_j^d\Big) \\ &\quad - |\Gamma_{e,i}|\boldsymbol{\tau}_i^d\delta_{ij} \quad \text{for all } i,j \in \mathcal{B}_e \end{aligned} \tag{B6a}$$

$$\begin{aligned} [\mathbf{K}_{\hat{u}\hat{p}}]_{i,j}^e &:= -|\Gamma_{e,i}||\Gamma_{e,j}|\boldsymbol{\tau}_i^d[\mathbf{A}_u^e]^{-1}\mathbf{n}_j + |\Gamma_{e,i}|\mathbf{n}_i\delta_{ij}\chi_{\mathcal{N}_e}(i) \\ &\quad \text{for all } i \in \mathcal{B}_e \text{ and } j \in \mathcal{A}_e \end{aligned} \tag{B6b}$$

$$[\mathbf{K}_{\hat{p}\hat{u}}]_{i,j}^e := -|\Gamma_{e,i}||\Gamma_{e,j}|\tau_i^p\,[\mathrm{a}_p^e]^{-1}\mathbf{n}_j^T \ \text{for all } i \in \mathcal{A}_e \text{ and } j \in \mathcal{B}_e \tag{B6c}$$

$$\begin{aligned} [\mathbf{K}_{\hat{p}\hat{p}}]_{i,j}^e &:= |\Gamma_{e,i}||\Gamma_{e,j}|\tau_i^p\,[\mathrm{a}_p^e]^{-1}\tau_j^p - |\Gamma_{e,i}|\tau_i^p\delta_{ij} \\ &\quad \text{for all } i \in \mathcal{A}_e \text{ and } j \in \mathcal{A}_e \end{aligned} \tag{B6d}$$

$$[\mathbf{f}_{\hat{u}}]_i^e := |\Gamma_{e,i}|\Big(\nu|\Omega_e|^{-1}\mathbf{N}_{\mathrm{V},i}^T\mathbf{f}^e{}_L - \boldsymbol{\tau}_i^d[\mathbf{A}_u^e]^{-1}\mathbf{f}^e{}_u\Big) - |\Gamma_{e,i}|\mathbf{g}_i\chi_{\mathcal{N}_e}(i) \quad \text{for all } i \in \mathcal{B}_e \tag{B6e}$$

$$[\mathbf{f}_{\hat{p}}]_i^e := |\Gamma_{e,i}|\tau_i^p\,[\mathrm{a}_p^e]^{-1}\mathrm{f}^e{}_p, \text{for all } i \in \mathcal{A}_e \tag{B6f}$$

for $e = 1, \ldots, \mathrm{n_{el}}$, with δ_{ij} being a Kronecher delta. Note that while $\mathbf{K}_{\hat{u}\hat{u}}$ and $\mathbf{K}_{\hat{p}\hat{p}}$ are symmetric, the global matrix in Equation (B5) is not, contrary to the FCFV formulation [8]. Moreover, following the conjecture introduced in Section 5, the matrix in Equation (B5) is expected to be negative definite, whereas the matrix of the global problem in the FCFV formulation [8] features a saddle point structure.

Finally, if a pure Dirichlet boundary value problem is considered, constraint (5) needs to be included in the above system. At the discrete level, this yields the additional equation

$$\sum_{e=1}^{\mathrm{n_{el}}} |\Omega_e| \mathrm{p}_e = 0 \tag{B7}$$

which is accounted for by introducing a Lagrange multiplier λ. Hence, the resulting system is

$$\begin{bmatrix} \mathbf{K}_{\hat{u}\hat{u}} & \mathbf{K}_{\hat{u}\hat{p}} & \mathbf{K}_{\lambda\hat{u}}^T \\ \mathbf{K}_{\hat{p}\hat{u}} & \mathbf{K}_{\hat{p}\hat{p}} & \mathbf{K}_{\lambda\hat{p}}^T \\ \mathbf{K}_{\lambda\hat{u}} & \mathbf{K}_{\lambda\hat{p}} & 0 \end{bmatrix} \begin{Bmatrix} \hat{\mathbf{u}} \\ \hat{\mathbf{p}} \\ \lambda \end{Bmatrix} = \begin{Bmatrix} \mathbf{f}_{\hat{u}} \\ \mathbf{f}_{\hat{p}} \\ \mathrm{f}_{\lambda} \end{Bmatrix} \tag{B8}$$

with

$$[\mathbf{K}_{\lambda\hat{u}}]_j^e := -|\Gamma_{e,j}||\Omega_e|[\mathrm{a}_p^e]^{-1}\mathbf{n}_j^T \qquad \text{for all } j \in \mathcal{B}_e \tag{B9a}$$

$$[\mathbf{K}_{\lambda\hat{p}}]_j^e := |\Gamma_{e,j}||\Omega_e|[\mathrm{a}_p^e]^{-1}\tau_j^p \qquad \text{for all } j \in \mathcal{A}_e \tag{B9b}$$

$$[\mathrm{f}_{\lambda}]^e := |\Omega_e|[\mathrm{a}_p^e]^{-1}\mathrm{f}_p^e \tag{B9c}$$